UTRECHT UNIVERSITY

BACHELOR THESIS

Study of charm jet momentum distribution in Pb-Pb collisions at $\sqrt{s_{NN}} = 2.76$ TeV

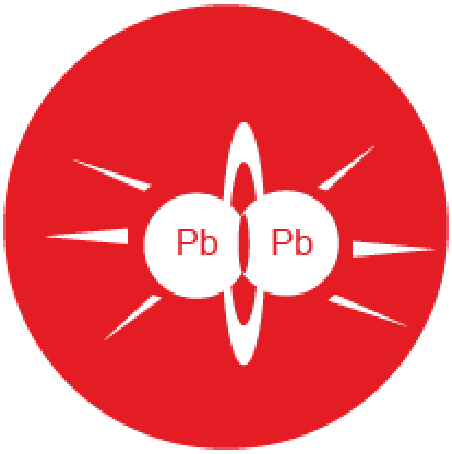

Author:
Sanne LOTH
Studentnumber 4113799
Utrecht University

Supervisors:
dr. André MISCHKE
and
dr. Barbara TRZECIAK
Utrecht University

15 June 2016

Abstract

The Quark-Gluon Plasma is a state of matter that is expected to form at high temperatures and densities. Therefore, it is expected to be produced in lead-lead ion collisions in ALICE at CERN. Jets, consisting of fragments of the heavy quarks produced during these collisions, can be used to study this medium. Specifically, jets containing D^0-mesons are considered.

The aim of this study is to assess the systematic uncertainty in the charm jet transverse momentum distribution in lead-lead ion collisions at $\sqrt{s_{NN}} = 2.76$ TeV. Two procedures, called the purple and orange to distinguish them, are developed and described thoroughly. In both cases, the jet transverse momentum distribution is determined using information from the invariant mass distribution of $(K\pi)$ pairs. The main difference between the two procedures is the moment of correction for the efficiency due to selection cuts and detector effects.

The procedures are applied to obtain the jet transverse momentum distribution for four different sets of selection cuts. Additional cuts in D^0 transverse momentum were needed in the purple procedure to remove background influence and improve the jet transverse momentum distribution. The same cuts were applied in the orange procedure.

Subsequently, the distributions are studied and compared.

The obtained jet transverse momentum distribution for all four selection cut sets are not consistent for both procedures. The distributions for the four sets resulting from the orange procedure do have similar shapes. The systematic uncertainty is in the order of 10^{-3} $(\mathrm{GeV}/c)^{-1}$.

The obtained results from the orange and purple procedure are also compared to each other. The jet transverse momentum distributions are not consistent; the systematic uncertainty depends on the selection cut set used.

Further examination of the purple procedure is recommended, since fluctuations, enhanced by the correction for efficiency, play an important role.

---

[0] The figure on the frontpage is a diagram of lead-lead ion collisions. [1]

Contents

Chapter 1

Introduction

The world of particle physics is very small: a typical length scale is 10^{-18} m (an attometer). On a first look, the same is true for energies: they are typically in the order of MeV ($\sim 10^{-13}$ J) or GeV ($\sim 10^{-10}$ J) [2]. However, this is a lot of energy relative to the size of the particle. As small as these numbers might be, the case is entirely the opposite for the number of particles created in the Large Hadron collider (LHC) after lead-lead ions collide onto each other. There are several million events registered.

In these lead-lead ion collisions, heavy quarks are produced. The D^0 particle is a fragment of such heavy quarks. It is a charmed meson, meaning that contains a charm quark. Also, a Quark-Gluon Plasma is expected to form for a short while following the collisions. This plasma is a hot, dense medium in which the quarks are free and with which they interact. The D^0-meson can be used to study the primary quarks and the plasma. One way to do this is to study the charm jet transverse momentum distribution.

The goal of this study is to determine if and how the resulting charm jet transverse momentum distribution depends on the selection cut set. Data is taken from ALICE, A Large Ion Collider Experiment. This is an experiment at the LHC. Two methods of analysing the data are also developed and compared. The aim is to determine the following:

- How stable the resulting transverse momentum distribution of the charm jet is under different sets of selection cuts.
- How stable the resulting jet transverse momentum distribution is under the two different procedures.
- What the influence of the efficiency correction is.

The fully corrected[1] jet tranverse momentum distributions for the selection cut sets are expected to be the same. Next to that, the distributions will ideally be the same for the two procedures: the method of analysis should not matter when the same cuts are applied during the analysis.

Investigating these properties will lead to the assessment of the systematic uncertainty in the jet transverse momentum distribution due to the used procedure and selection cut set.

Before discussing this methods and the obtained results, an introduction to particle physics will be given in Chapter 2. The focus lies on Quantum Chromodynamics, including the production of heavy quarks and the influence of the Quark-Gluon Plasma.

The experimental set-up and analysis are described in Chapter 3. First, the relevant subsystems of the ALICE detector are described. After that, the process of analysing the data set is explained: first reconstructing the D^0-meson and the jet, after that, two different procedures for obtaining jet transverse momentum distributions.

The results are presented in Chapter 4. In Chapter 5, the obtained results will be discussed and the resulting jet transverse momentum distributions are compared. The conclusions will be presented in Chapter 6.

---

[1] Fully corrected means corrected for: the efficiency of the selection cuts, the number of selected events and additional cuts made during the analysis procedure.

Chapter 2

Background

2.1 Introduction to Particle Physics

Humans have always wondered what the world is made up of. Theories about the constituents of the world go centuries back. For instance in ancient Greece, where Leucippus and his apprentice Democritus suggested the world was made up of indivisible particles: atoms. Plato felt the concept of atoms did not describe the beauty seen in the world. Instead he theorised the world was made up of four geometric solids each denoting an element: fire, air, water and earth [3].

The discovery of the electron in 1897 by J.J. Thomson could be taken as the birth of elementary particle physics. Rutherford showed in a scattering experiment that most of the mass and the positive charge of the atom was at the center of the atom: the nucleus. He named the hydrogen nucleus ”proton”. In 1932, Chadwick discovered the neutral part of heavier nucle:, the neutron [4].

In the mid 20^{th} century, research was done into propositions of particles that differed greatly from the atom. Yukawa proposed another force which bound the protons and neutrons together, overcoming charge repulsion, namely the strong force. Moreover, Planck made a first step towards finding the photon when he theorised electromagnetic radiation should be quantized. But he could not explain why this should be true. Einstein famously suggested the quantisation was due to the particle-like nature of light. His suggestion was confirmed in experiments by Milikan and later by Compton [4].

Throughout the 20^{th} century, more particles were discovered. This led to the creation of the Standard Model of particle physics, in which particles and force carriers describe the world around us. The interaction of particles and force carriers results in forces. As shown in figure 2.1, there are twelve elementary particles. The quarks (shown in purple in figure 2.1) have fractional elementary charge. The leptons (shown in green) have elementary charge e. Both quarks and leptons come in three generations. The different types of quarks and leptons are called ”flavours”. All elementary particles also have corresponding anti-particles. They have the same mass and spin, but all other quantum numbers (e.g. charge) are opposite [2].

The force carriers (shown in red) are the gluon (strong force), photon (electromagnetic force) and the Z^0 and $W^{\pm}$ bosons (weak force). Gravity cannot be described within the Standard Model of particle physics. Therefore, it is not complete. Lastly, the Higgs Boson (denoted in yellow) is the particle responsible for giving particles their mass [6].

The ordinary matter is made up of the lighter particles: the up and down quarks and electrons. The heavier particles are not very stable and therefore play a smaller role in everyday life. For instance the charmed meson D^0 has a lifetime of approximately $4 \cdot 10^{-13}$ s [7]; a proton is expected to have finite lifetime of at least 10^{34} years. Note that the universe has existed for roughly 10^{10} years.[1]

---

[1] Protons are expected to decay in some Grand Unified Theories, but no one has measured this yet [8].

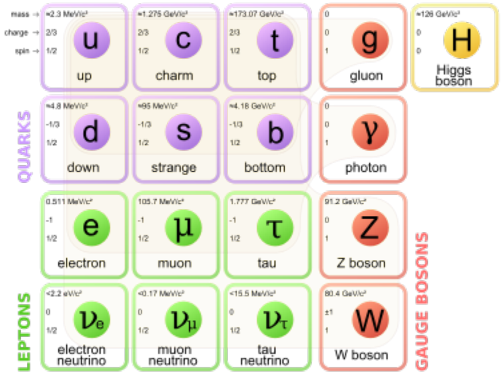

Figure 2.1 – The Standard Model of particle physics. It contains six quarks, six leptons, four force carriers and the Higgs Boson [5].

2.2 Quantum Chromodynamics

Quantum Chromodynamics (QCD) is a theory of strong interactions between quarks and gluons, analogue to the electroweak theory.[2] Just like atoms are bound together by charge differences and are neutral outwardly, quarks are bound together by "colour". There are three colours; red, green and blue, and the respective anticolours. As an analogue to the photon, the gluon is the force carrier of colour. However, the gluon itself is coloured too, which leads to a more complex situation than for electromagnetism. Quarks form groups (hadrons) so that together they are colour-neutral. This is done in (at least) the following ways:

- **Mesons**: a quark+antiquark pair. Since all quarks can carry all three colours, a meson is a superposition of these colour pairs. An example is the neutral pion π^0, which has quark content $u\bar{u}$ or $d\bar{d}$. So for the $u\bar{u}$ state: $\frac{1}{\sqrt{3}}\,[u_r\bar{u}_{\bar{r}} + u_g\bar{u}_{\bar{g}} + u_b\bar{u}_{\bar{b}}]$.
- **Baryons**: a group of three quarks. Famous examples are the proton (uud) and the neutron (udd).
- **Tetraquark**: a group of four quarks. Researchers have found states of the form $q\bar{q}Q\bar{Q}$ and a form with four different flavours. It is not yet understood if the latter form is indeed one group or two mesons tightly locked together [9].
- **Pentaquark**: the pentaquark is made up of five quarks. Studies such as [10] and [11] have found results consistent with theoretical properties of pentaquarks.

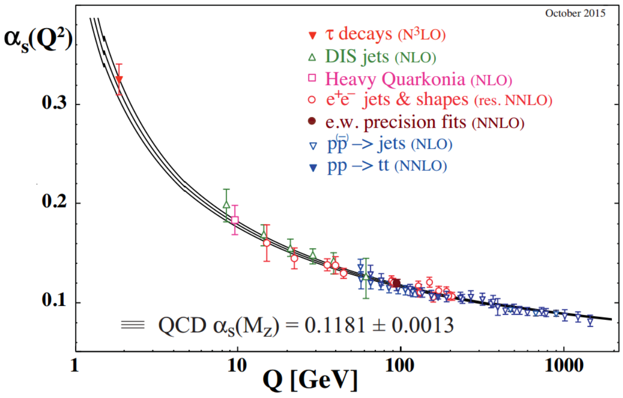

Figure 2.2 – Comparison of measured α_s values to theoretical models [12].

---

[2] This section is based on [2].

The strong force is described by the potential

$$V = -\frac{4}{3}\frac{\alpha_s(r)}{r} + kr, \tag{2.2.1}$$

where k is the QCD string tension and α_s the running coupling constant. It is important to note that α_s is not constant at all. It depends on distance and momentum transfer. Figure 2.2 compares measurements of α_s with several theoretical models based on pertubation QCD. This shows that α_s is small when the transferred momentum is large (or therefore when the distance is small), which corresponds to hard processes. If the transferred momentum decreases (distance increases), α_s increases. The result is that the quarks are asymptotically free [12]. At small distances, both terms in equation 2.2.1 are very small, meaning that the strong force is actually weak. Here, the quarks are not bound that strongly to each other. A proposed situation is the Quark-Gluon Plasma, further described in section 2.4.

At very large distances, the strong force is very strong. The consequence is that quarks are confined to hadrons. When quarks within a hadron are separated, the potential increases till a critical distance. At this point, there is enough energy to create a pair of light quarks. These quarks pair with the original quarks and are yet again in a hadron. This process is illustrated in figure 2.3.

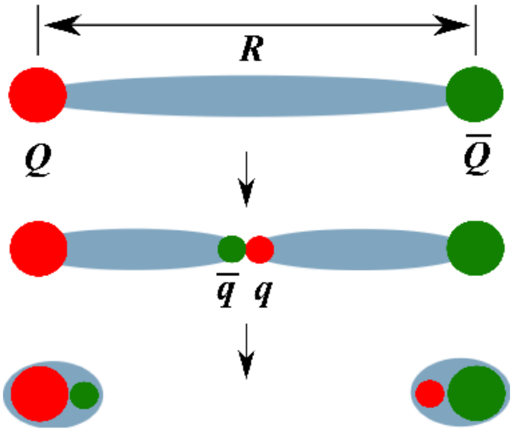

Figure 2.3 – When quarks in a hadron are separated, the strong force increases in order to keep them confined. At some critical distance, the QCD string between them snaps and a quark pair $q\bar{q}$ is formed. They pair with Q and $\bar{Q}$, again forming a colourless hadron [13].

2.3 Heavy Quark Production

The production and hadronization of heavy quarks is discussed in [14]. Light quarks can originate from many sources in hadron-hadron collisions: valence flavours, pertubative subprocesses and nonpertubative hadronization. Since they can have so many different origins, measuring light quarks does not give much information about the initial stages after the collisions.

However, heavier quarks (c, b, t^3) have masses above the Λ_{QCD} scale[4]. They can be described by pertubative QCD, which are calculations that can be done and thus data can be compared to theoretical descriptions. Since they are mostly produced at the initial stages of the collisions and thus have high momenta, they are hard probes. The heavy quarks radiate gluons and at some point fragment. This sets a cascade of particles being formed into motion. This cascade is called a jet. Hadrons with a major share of their original quark's energy are expected to describe their original quarks well in terms of direction and momentum, though their momentum may be lower due to energy loss.

---

[3] Note that top does not live long enough to form hadrons. [14]

[4] This is about 200 MeV.

Heavy quarks can be produced in hadron-hadron collisions in the following ways:

- **Pair creation** (figure 2.4a): a leading order process, described by $gg \to Q\bar{Q}$ or $q\bar{q} \to Q\bar{Q}$. $Q, \bar{Q}$ are produced back to back.
- **Flavour excitation** (figure 2.4b): a heavy particle scatters off a parton of another beam and is excited. The process is essentially $Qq \to Qq$ and $Qg \to Qg$.
- **Gluon splitting** (figure 2.4c): this can happen at the initial- or final-state shower. The process is $gg \to Q\bar{Q}$. It's mostly found at final-state-showers, since splitting at the initial-state mostly results in flavour excitation. This is considered a soft process [15].

Pair creation is the dominant process at lower energies. The relative contribution of gluon splitting increases as the energy increases and at very high energies ($\sim 10^4$ GeV) gluon splitting may even dominate the production [14].

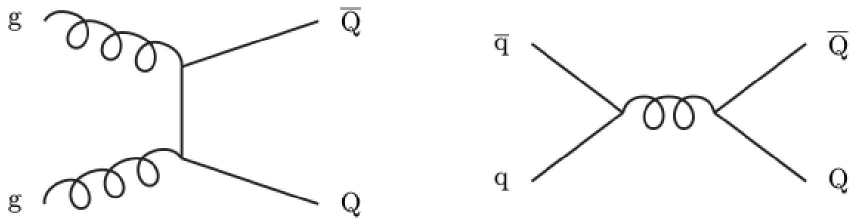

(a) Pair creation via the processes $gg \to Q\bar{Q}$ and $q\bar{q} \to Q\bar{Q}$.

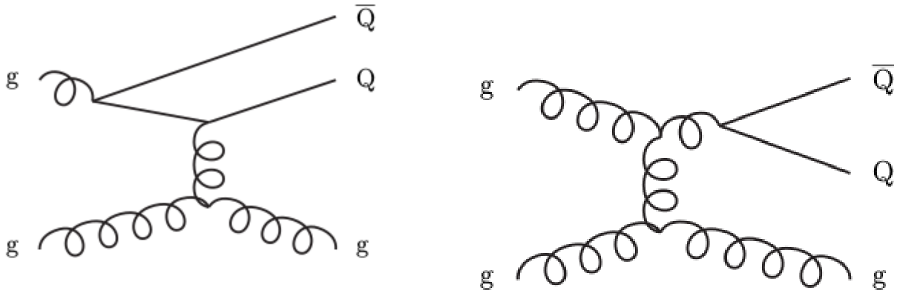

(b) Flavour excitation: excitation of a quark by scattering via the process $Qq \to Qq$ and $Qg \to Qg$.

(c) Gluon splitting: one gluon splits into a quark pair via the process $g \to Q\bar{Q}$.

Figure 2.4 – Production of heavy quarks using pertubative QCD [14].

As mentioned, the focus lies on the charmed meson D^0 (and its antipart $\bar{D}^0$), containing either $c\bar{u}$ (or $u\bar{c}$). The decay chain considered is:

$$D^0 \to K^{\pm}\pi^{\mp} \tag{2.3.1}$$

with a branching ratio $3.89 \pm 0.05\%$ [16]. The D^0 is a fragment from a charm quark. Studies have shown that D^0 carries a major amount of its jet's energy, which is expected for a jet coming from primary $c, \bar{c}$ quark pair. Thus, studying D^0 mesons gives a good impression of the original charm quark and can therefore give information about the initial stages after a collision. If the charm quark was produced by pair creation, a similar anti-charm jet can be found going in the opposite direction [15].

The momenta of both the D^0 meson and its jet can be determined. The ratio of their momenta (energy) can then be calculated. This is the fragmentation function z. An example of z can be found in figure 2.5. Soft processes (particles with low momenta) expectedly have a low value of z whereas hard processes (particles with high momenta) have a high value of z.

The fragmentation function shows how much momentum of the jet (and thus the original quark) is carried by the D^0-meson. Since the production of charm quarks is not fully understood, the z distribution gives more information about charm and how its momentum is distributed to its fragments. However, the z distribution is not often used since this would lead to unfavourable statictics. Often there are not many entries in a z distribution.

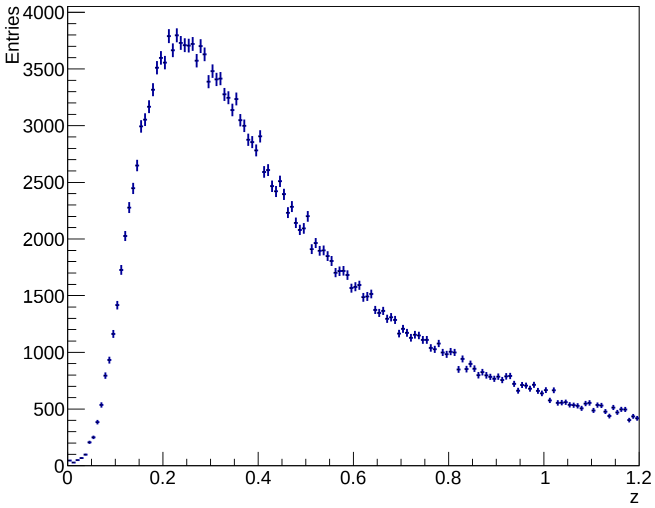

Figure 2.5 – Example of a distribution of the fragmentation function z: the ratio of D^0 p_T and D^0 jet p_T.

2.4 Quark-Gluon Plasma

As mentioned in section 2.2, single quarks are not observed. However, it is believed that in the very early universe ($\sim 10^{-6}$ s), temperatures and quark densities were high enough for the quarks to be deconfined. This state of deconfinement was named "Quark-Gluon Plasma" (QGP). But the universe expanded, cooled down and as such, hadrons were formed [2].

Several experimental setups were built to study the QGP using high energy heavy ion collisions. The Relativistic Heavy Ion Collider (RHIC) at Brookhaven National Laboratory is one of these experiments. At RHIC, gold ions are mainly used to for heavy ion collisions. The top centre of mass energy is $\sqrt{s_{NN}} = 200$ GeV. The QGP was expected to be a weakly-coupled medium. However, the data points to a strongly coupled medium, which is present for a short while ($\sim 10^{-23}$ s). This medium has near ideal fluid properties [17].

The QGP is also studied at the Large Hadron Collider (LHC), where lead ions are collided onto each other to create hot and dense circumstances. The centre of mass energy of the LHC is currently about $\sqrt{s_{NN}} = 5.5$ TeV [1]. Heavy quarks such as charm are expected to form in the initial stages of the collision. This means they experience the whole evolution of the medium. The heavy quarks are also colour charged and therefore interact with the medium[5] [18].

---

[5] For instance a photon is not colour charged and does not interact with the medium.

They lose energy while travelling through the medium in the following ways:

- **Elastic scattering**: the quarks interacts with the medium by collision. It consequently loses energy. The longer a particle travels through the medium, the more energy it can lose.
- **Gluon radiation**: in the presence of the medium, quarks may radiate gluons and as a result lose energy. Note that this energy loss differs per flavour due to the dead cone effect. At small angles gluons cannot be radiated. Thus, a radiation free cone is formed around the particle. This angle depends on the mass of the quark. The heavier the quark, the less energy it loses. Again, the longer a particle travels through the medium, the more energy it loses.

The same is true for the jets coming from these heavy quarks. The primary quarks interact with the QGP, lose energy and radiate gluons. The gluons can also interact with the QGP. Since its constituents are altered by the QGP, the jet's energy and momentum distribution will be altered too, compared to proton-proton collisions.

Jets can also be produced back-to-back. If they are produced closer to the "edge" of the medium, one jet has to travel for a longer time through the medium than the other. This means that one jet will lose more energy than the other. It is possible that the charm quark and its fragments lose so much energy that a jet completely disappears. This is a process named "jet quenching" [19].

If the QGP exists, this results in a very different situation compared to proton-proton collisions where QGP is not expected to form. Thus, comparing to data from p-p collisions can show if there is a hot, dense medium formed after a collision of heavy ions. What actually happens in the medium of course depends on the properties of the QGP. Models, each with different assumptions about the QGP, are also compared to the data from heavy ion collisions to determine these properties.

Chapter 3

Experimental Setup and Analysis

The following sections will describe how the data is collected, reconstructed and analysed.

3.1 CERN

The European Organization for Nuclear Research (CERN) was founded in 1954 to study the properties of nuclei. Its first accelerator, the Synchrocyclotron, started up in 1957. As the knowledge of the world of particles expanded, the goal of CERN changed to testing the Standard Model of particle physics, researching fundamental particles and beyond. The first dive into particle physics came with the Proton Synchrotron in 1959. This accelerator briefly had the world's highest energy, at 28 GeV. Later, research headed towards anti-nuclei and anti-atoms. The Z and W particles were discoverd in 1983 [20].

Commissioned in 1989 and built in a 27 km circular tunnel, the Large Electron-Positron collider (LEP) closed in 2000 to pave way for the Large Hadron Collider (LHC). The LHC started up in 2008 and is still the largest, most powerful particle accelerator on Earth. Two particle beams, accelerated to nearly the speed of light, travel in seperate beam pipes before they collide. Superconducting magnets bend their tracks. They also focus and squeeze the beams, so the chance of a collision increases. The beams finally meet in one of the detectors: ALICE, ATLAS, CMS and LHCb [21].

In this experiment, lead-lead nuclei are accelerated in the LHC to near the speed of light. The used dataset is from collisions with a centre of mass energy of $\sqrt{s_{NN}} = 2.76$ TeV from ALICE.

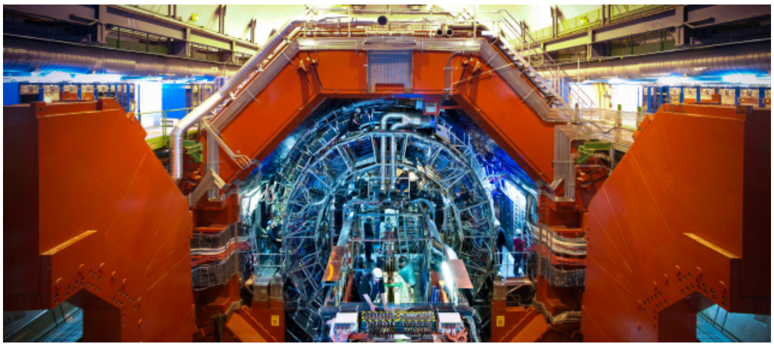

Figure 3.1 – ALICE detector [22].

3.2 ALICE

ALICE (A Large Ion Collider Experiment, shown in figure 3.1) has many subsystems to track particles and measure their properties. A full description of ALICE is given in [23]. Here, the subsystems relevant for the identification of the D^0-meson and its jet are outlined.

- **ITS** (*Internal Tracking System*): six tracking layers record tracks and measure the deposited charge, therefore providing a measurement of ionization energy loss dE/dx. This is mainly useful for low momenta; $p_T \lesssim 0.7$ GeV/c.

- **TPC** (*Time Projection Chamber*): a drift chamber with a volume of 90 m^3 to track charged particles. Similar to the ITS, it tracks the particles and it can also measure the ionization energy loss dE/dx. Next to that, it measures charge and momentum. In contrast to the ITS, the TPC can measure up to $p_T \sim 20$ GeV/c. The Bethe-Bloch formula describes the energy loss:

  $$f(\beta\gamma) = \frac{P_1}{\beta^{P_4}}\left(P_2 - \beta^{P_4} - \ln\left(P_3 + \frac{1}{(\beta\gamma)^{P_5}}\right)\right) \qquad (3.2.1)$$

  where β is the velocity of the particle, γ the Lorentz factor and $P_1 - P_5$ are fit parameters which depend on the particle type. For instance the parameters for kaons and pions differ, therefore their Bethe-Bloch curve will be distinguishable too. Thus, the Bethe-Bloch curve is used to identify the particle, as seen in figure 3.2.

- **TOF** (*Time of Flight*): an area array of Multigap Resistive Plate Chambers (MRPC) that measure the arrival time of particles. The resolution is about 80 ps for pions with a momentum around 1GeV/c. The velocity of particles is used to distinguish them: due to the different masses of particle types, the factor $\beta = v/c$ will differ. This method is more precise for particles with a lower velocity. At velocities near the speed of light, $\beta \approx 1$, making it difficult to distinguish between particle types.

In both the TPC and the TOF, measured particles are approximated with a gaussian. A 3σ cut is applied when determining what particle has been measured.

The measurements of these detectors are combined to enhance particle identification: the separation between particles is increased, making it easier to identify them.

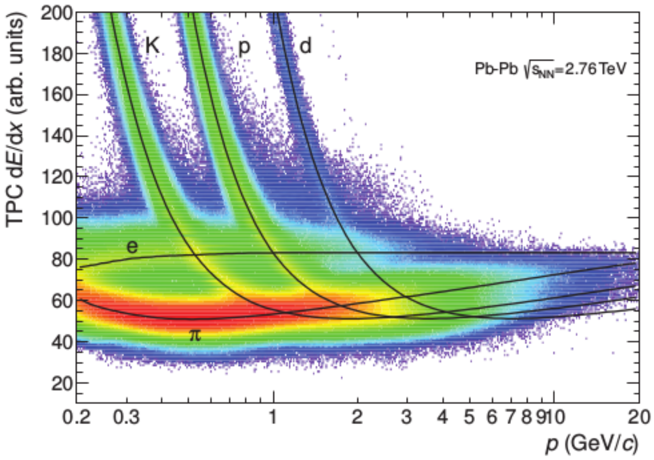

Figure 3.2 – An example of energy loss in the TPC. The lines reflect the curves from the Bethe-Bloch formula (equation 3.2.1) for different particle types [23].

3.3 Dataset

The used dataset is LHC11h from 2011. The data is comprised of two sets of runs. The TPC Good Runs are uniform in the azimuthal distribution. The TPC Semi-Good Runs have a deviation in some azimuthal region. For the TPC Semi-Good Runs, there are two subcases: one where the IROC13 had a lower voltage (resulting in a dip in the ϕ distribution), and one where the OROC-C08 was turned off [15].

TPC Good Runs: 167903, 167915, 167987, 167988, 168066, 168068, 168069, 168076, 168104, 168107, 168108, 168115, 168212, 168310, 168311, 168322, 168325, 168341, 168342, 168361, 168362, 168458, 168460, 168461, 168464, 168467, 168511, 168512, 168777, 168826, 168984, 168988, 168992, 169035, 169091, 169094, 169138, 169143, 169144, 169145, 169148, 169156, 169160, 169167, 169238, 169411, 169415, 169417, 169835, 169837, 169838, 169846, 169855, 169858, 169859, 169923, 169956, 170027, 170036, 170081

TPC Semi-Good Runs 1 (IROC-C13 low voltage): 169975, 169981, 170038, 170040, 170083, 170084, 170085, 170088, 170089, 170091, 170152, 170155, 170159, 170163, 170193, 170195, 170203, 170204, 170228, 170230, 170268, 170269, 170270, 170306, 170308, 170309

TPC Semi-Good Runs 2 (OROC-C08 turned off): 169591, 169590, 169588, 169587, 169586, 169584, 169557, 169555, 169554, 169553, 169550, 169515, 169512, 169506, 169504, 169498, 169475, 169420, 169418, 169099, 169040, 169045, 169044

Only the 10 % most central events are used. The central trigger system of ALICE is based on the Silicon Pixel Detector (SPD) and two V0-detectors [23]. Next to that, only events were selected whose primary vertex have a displacement of ±10 cm from the centre of the detector with respect to the beam direction.

3.4 Reconstructing D^0-meson

The D^0-meson is reconstructed from its decay to pions and kaons (see equation 2.3.1).

The dataset is first analysed using four different sets of selection cuts: "central", "tighter", "looser" and "AR"[1]. The looser and tighter selection cuts are variations of the central selection cuts.

The tighter cuts have the following changes:

- **DCA**: 0.010 cm is subtracted from the central cut DCA value.
- $(d_0^k d_0^\pi)$: 15% of the central cut value is added.
- $|\cos(\theta_{point})|_{XY}$: 0.05 is added to the central cut value. However, the maximum possible value for the tighter cut is 0.98.

For the looser cut set, these changes are:

- **DCA**: 0.015 cm is added to the central cut DCA value.
- $(d_0^k d_0^\pi)$: 15% of the central cut value is subtracted.
- $|\cos(\theta_{point})|_{XY}$: 0.05 is subtracted from the central cut value.

The central selection cuts are shown in table 3.1. The tables with the selection cuts for looser, tighter and AR are given in Appendix I.

The selection cuts are based on the topological displacement of the secondary vertex from the primary vertex. The typical displacement is $c\tau = 123\ \mu$m, which is a measurable length. There are also kinematic cuts on the momenta of the pions and kaons. A lot of pions and kaons are produced in the collisions, but they mostly have lower momenta. Therefore, the cuts in 3.1 are more strict for lower D^0 p_T.

---

[1] This is a set of selection cuts made by Andrea Rossi [24].

D^0 p_T (GeV/c)	2-3	3-4	4-5	5-6	6-8	8-12	12-16	16-20	20-24	24-∞
Δm_{D_0} (GeV/c^2)	0.40	0.40	0.40	0.40	0.40	0.40	0.40	0.40	0.40	0.40
DCA (cm)	0.025	0.025	0.025	0.025	0.030	0.035	0.040	0.040	0.040	0.040
$\cos(\theta^*)$	0.8	0.8	0.8	0.8	0.8	1.0	1.0	1.0	1.0	1.0
K p_T (GeV/c)	0.7	0.7	0.7	0.7	0.7	0.7	0.7	0.7	0.7	0.7
π p_T (GeV/c)	0.7	0.7	0.7	0.7	0.7	0.7	0.7	0.7	0.7	0.7
$\lvert d_0^K \rvert$ (cm)	0.1	0.1	0.1	0.1	0.1	0.1	0.1	0.1	0.1	0.1
$\lvert d_0^\pi \rvert$ (cm)	0.1	0.1	0.1	0.1	0.1	0.1	0.1	0.1	0.1	0.1
$d_0^k d_0^\pi$ (10^{-4} cm^2)	4.5	3.6	2.7	2.1	1.4	0.50	0.10	0.10	0.10	0.10
$\cos(\theta_{point})$	0.95	0.95	0.95	0.92	0.88	0.85	0.83	0.82	0.82	0.82
$\lvert\cos(\theta_{point})\rvert_{XY}$	0.998	0.998	0.998	0.998	0.998	0.998	0.998	0.998	0.998	0.998
L_{XY}	7	5	5	5	5	5	8	6	6	6

Table 3.1 – Central selection cuts for D^0 of the 10% most central events.

The pions and kaons were identified using information from the TPC and TOF. The invariant mass of all possible pion-kaon combinations is determined using the invariant mass relationship

$$m^2c^4 = (\sum_{i=1}^{n} E_i)^2 - (\sum_{i=1}^{n} \vec{p}_i)^2 \tag{3.4.1}$$

and conservation of energy and momentum. This results in a mass peak around the D^0 mass (from the correct pairs, coming from D^0) and background in the form of a slope (coming from the incorrectly combined pairs). This can be seen figure 3.3.

Due to the selection cuts when analysing the raw data and due to detector performance, there is an efficiency in actually finding the D^0-meson. The efficiency of measuring the D^0 is determined using Monte-Carlo simulations. In this simulation, the true number of D^0-mesons is known. By setting the selection cuts and detector specifications, one can determine how many D^0-mesons are detected. This results in an efficiency distribution.

The efficiency differs for per range of D^0 p_T. Due to the efficiency, any distribution where D^0 plays a role ought to be corrected in order to take this into account. The efficiencies for each of the four sets of selection cuts are shown in figure 3.4.

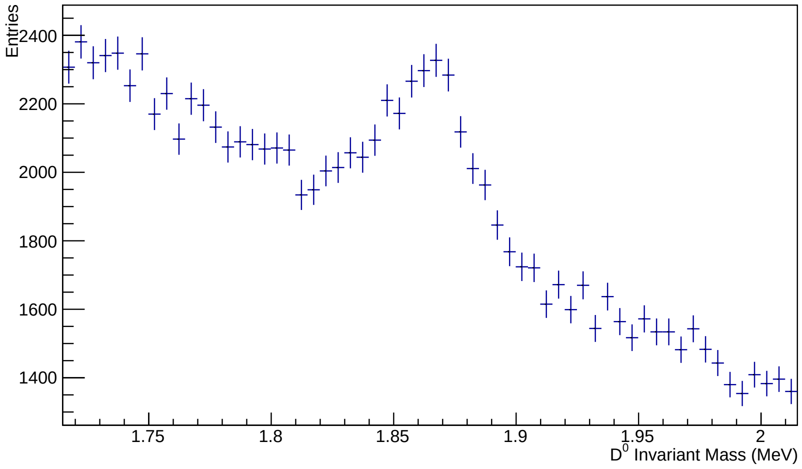

Figure 3.3 – Example of an invariant mass distribution of (Kπ) pairs.

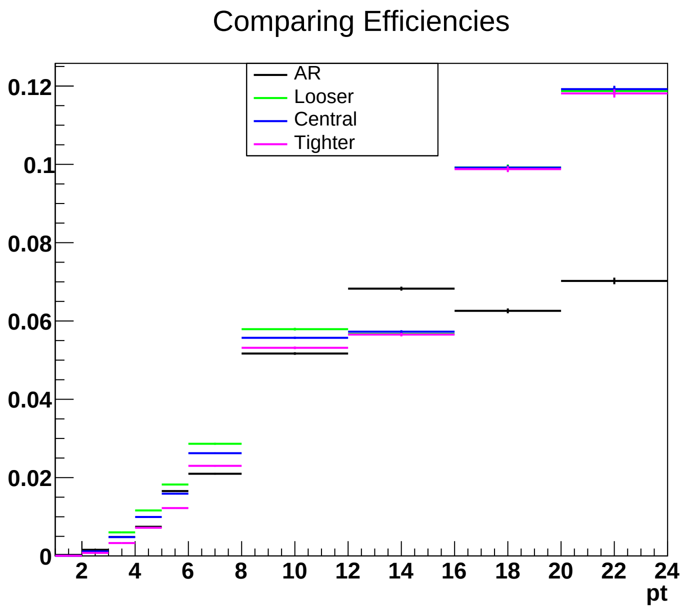

Figure 3.4 – Efficiency of measuring D^0 for different ranges of D^0 p_T for four different sets of selection cuts.

3.5 Reconstructing Jets

A jet is a cone consisting of many particles which are formed when a primary quark fragments. They are reconstructed using the **FASTJET3** package [25]. Jets are found with the anti-k_t algorithm [26]:

$$d_{ij} = \min\left(\frac{1}{p_{ti}^2}, \frac{1}{p_{tj}^2}\right) \Delta R_{ij}^2/R^2 \tag{3.5.1}$$

$$d_{iB} = \frac{1}{p_{ti}^2}, \tag{3.5.2}$$

where $\Delta R_{ij}^2 = (y_i - y_j)^2 + (\phi_i - \phi_j)^2$. p_{ti} is the tranverse momentum of particle i, y_i its rapidity and ϕ_i its azimuthal angle. d_{iB} is the distance to the beam. R is a parameter that has to be set; it is usually in the order of 1.

In this algorithm, the minimum distance of all d_{ij} and d_{iB} is determined. If this minimum distance corresponds to two particles, those two particles are merged into one new particle using the relationship between energy, momentum and mass (equation 3.4.1). The new particle remains in the list.

If the minimum distance is from a particle to the beam, then the particle is part of a jet and taken out. This process continues until there are no particles left: all particles will be part of a jet. The final situation is illustrated in figure 3.5.

The anti-k_t algorithm is defined in such a way that particles with higher momenta are selected first. Around those hard particles, the jet is build up in a conical method. The soft particles do not influence the shape of the jet, whereas hard particles do.

Background is approximated with the k_t algorithm:

$$d_{ij} = \min\left(p_{ti}^2, p_{tj}^2\right) \Delta R_{ij}^2/R^2 \tag{3.5.3}$$

$$d_{iB} = p_{ti}^2. \tag{3.5.4}$$

The algorithm works the same way as the anti-k_t algorithm, but in this case it starts with particles with lower momenta. This means that soft particles are clustered first. This makes the algorithm ideal to approximate background of the hard particles.

Nevertheless, reconstructing jets is not easy since there are many particles created in heavy ion collisions. What is jet and what is background is more difficult to distinguish than in a situation with fewer particles being formed, such as p-p collisions. This

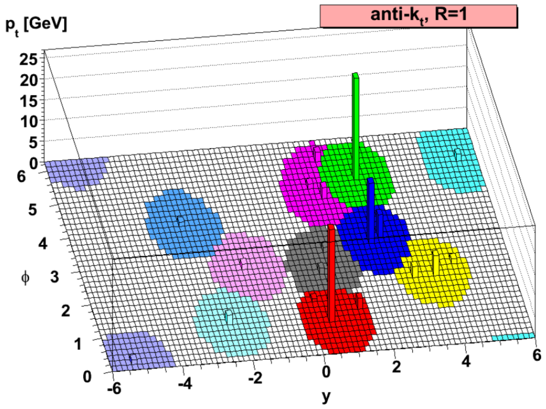

Figure 3.5 – An illustration of reconstructed jets using the anti-kt algorithm. The different jets are shown in different colours [26].

uncertainty leads to a smearing of the reconstructed tracks of particles and thus of reconstructed jets. Detector resolution also plays a role in this [23]. Section 3.7 outlines how this problem is tackled.

3.6 Data Analysis

Two procedures are used in the data analysis, labelled by a colour in order to distinguish them: the purple procedure and the orange procedure. These are described in Subsections 3.6.1 and 3.6.2, respectively. First, I will discuss the general outline of the analysis.

The analysis is done using the frameworks ROOT and AliRoot. ROOT is an object-oriented framework made by CERN to process and analyse large amounts of data. AliRoot is a framework that is based on ROOT, made for analysing data from ALICE specifically.

The invariant mass distribution in figure 3.3 is combined with the distributions of jet momentum and D^0 momentum. This results in a 3D histogram, of which an example is given in figure 3.6. A more refined result for one of the axis (D^0 mass, D^0 or jet p_T) can be obtained by projecting the other two axes to that axis.

The result of the projection to the D^0 mass axis is fitted using *AliHFMassFitter*. Several options have to be set. The minimum and maximum value on the x-axis are chosen around the expected D^0 mass. Background is fitted with an exponential function:

$$f(x) = e^{c_0+c_1x}, \tag{3.6.1}$$

where c_0, c_1 are parameters determined during the fit. Signal is fitted with a gaussian:

$$f(x) = \frac{c_3}{\sigma\sqrt{2\pi}}e^{-\frac{(x-\mu)^2}{2\sigma^2}}, \tag{3.6.2}$$

where μ (D^0 mass) and σ are given by the initial values set in the macro. c_3 is a parameter determined during the fit. These values are kept the same throughout the analysis and can be found in table 3.2.

mass	1.855 GeV/c^2
sigma	0.01 GeV/c^2
lower mass threshold	1.71 GeV/c^2
higher mass threshold	2.1 GeV/c^2

Table 3.2 – Initial values for fitting an invariant mass distribution of a (Kπ) pair.

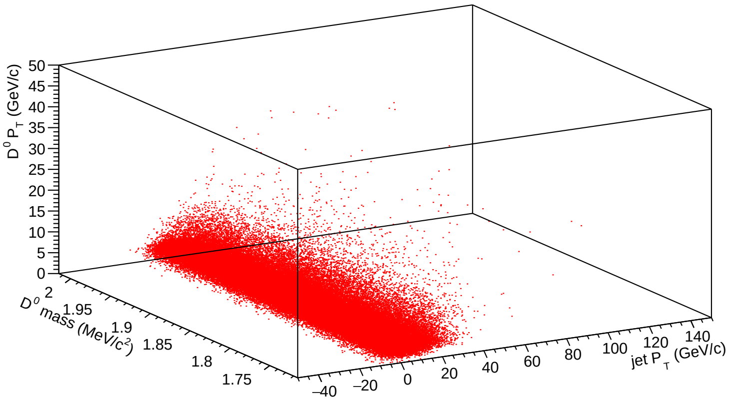

Figure 3.6 – A 3D histogram combining jet p_T, D^0 p_T and D^0 mass.

Parameters that are extracted are:

- **Mean mass**: the mean value of the gaussian signal peak in the invariant mass distribution.
- **Sigma**: the broadness of the signal peak.
- **Significance**: shows whether the resulting mass peak is a fluctuation, or significantly different from the background. This is shown in amounts of sigma. A significance of 3σ and higher is considered a relevant measurement.
- **Signal over background ratio**: the amount of signal (mass peak) relative to the background under the gaussian signal peak.
- **Signal yield**: amount of entries for each jet p_T bin.

The jet p_T spectrum is determined from the signal yield: for each bin, this is the number of entries divided by the bin width (dN/dp_T). The aim of this analysis is to determine the jet p_T spectrum, which is relevant when studying the presence and properties of the QGP.

For both procedures D^0 p_T ranges from 2 to 12 GeV/c and jet p_T from -20 to 23 GeV/c. The ranges of jet p_T and D^0 p_T are divided in several bins. For jet p_T (in GeV/c), the bins are:

$$[-20, -10),\ [-10, -5),\ [-5, 0),\ [0, 5),\ [5, 10),\ [10, 12),\ [12, 16),\ [16, 19),\ [19, 23).$$

There are bins containing negative transverse momentum. These are due to the subtraction of the background. The range $[23, \infty)$ is cut since it contains very few entries.

For D^0 p_T, the bins (in GeV/c) are the following:

$$[2, 3),\ [3, 4),\ [4, 5),\ [5, 6),\ [6, 8),\ [8, 12).$$

Note that D^0 p_T starts from 2 GeV/c. The range $[0, 2)$ GeV/c has very little signal is mostly made up of background. The range $[12, \infty)$ is also cut out: there are very few entries ($\propto 10$) in this range that do not add to the analysis in a meaningful way.

3.6.1 Purple Procedure

This procedure starts from a 3D histogram using jet p_T, D^0 p_T and D^0 mass axes. For a selected jet p_T bin:

- For one D^0 p_T bin, the invariant mass distribution is determined by doing a projection of the jet p_T and D^0 p_T axes to the D^0 mass axis. An example of an invariant mass distribution of $K\pi$ pairs is shown in figure 3.7.
- The invariant mass distribution of this D^0 p_T bin is scaled by 1/efficiency of that bin in order to correct for the efficiency.
- These two steps are repeated for all 6 D^0 p_T bins. Then, they are added up.
- The resulting invariant mass distribution is fitted with the initial values in table 3.2. The signal is fitted with a gaussian (equation 3.6.2). The background is fitted with an exponential (equation 3.6.1).
- From this fit, the mean mass, sigma, signal yield and signal over background ratio are extracted.
- The signal yield is divided by the width of this jet p_T bin. This is an entry to the jet p_T distribution.

This process is repeated for all jet p_T bins. Therefore, for each jet p_T bin there is an invariant mass distribution. For each parameter, there is a graph or histogram with the values for each jet p_T bin. The results of this procedure can be found in section 4.1.

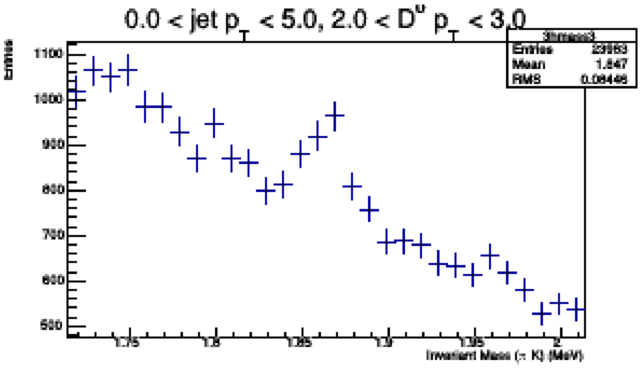

Figure 3.7 – Example of an invariant mass distribution in one D^0 p_T and one jet p_T bin.

3.6.2 Orange Procedure

This procedure starts from the same 3D histogram as in the previous procedure: it uses jet p_T, D^0 p_T and D^0 mass. For a selected D^0 p_T bin:

- The entire range of jet p_T and that one D^0 p_T bin are projected to the mass axis. This results in an invariant mass distribution.
- The invariant mass distribution is fitted with a gaussian for the signal (equation 3.6.2) and an exponential for the background (equation 3.6.1). The mean and sigma from the gaussian fit are extracted.
- Two regions are defined: [signal with background] and [sideband]. [Signal with background] has a width of 3 sigma around the mean of the gaussian. [Sideband] is the area *outside* a width of 4 sigma around the mean. This is illustrated in figure 3.8a: [signal with background] is shown in red, [sideband] is shown in blue.

- Thus, there are two regions: [signal with background] and [sideband]. For [signal with background], the mass range is mean±3sigma. [Sideband] contains two regions: [lower sideband], ranging from the minimum mass bin to mean−4sigma; [upper sideband], ranging from mean+4sigma to the maximum mass bin.
- The number of entries for the background under the gaussian signal peak is extracted from the fit. In figure 3.8a, this is the number of entries in the red region beneath the red line of the exponential function.
- For the [signal with background] region: the mass axis (for its mass range as described above) and D^0 p_T bin are projected to the jet p_T axis. This results in a yield histogram for the [signal with background] region. This is shown in figure 3.8b in blue.
- The same is done for [lower sideband] and [upper sideband]. The yields of these two regions are added up. Then, the number of entries of the [sideband] yield is rescaled such that is has the same number of entries as the background underneath the gaussian signal peak. This is shown in figure 3.8b in red.
- The yield of [rescaled sideband] is subtracted from the yield of [signal with background]. This results in the yield of [signal] only. The [signal] yield is corrected for bin width (dN/dp_T). An example is shown in figure 3.8c.

This is process is repeated for all D^0 p_T bins. In the end, there is an invariant mass distribution and jet p_T distribution for each D^0 p_T bin. The jet p_T distributions are corrected for efficiency and added up, resulting in one final jet p_T distribution. These results can be found in section 4.2.

3.7 Unfolding

For the full analysis, the jet p_T spectra obtained in the analysis should be unfolded. As mentioned in section 3.5, the data is smeared due to uncertainties in background and signal and due to finite precision of the detectors. Therefore, the jet p_T spectra of the above procedures is not the ”real” outcome. To get closer to the ”real” result, unfolding is used: this is a method to statistically remove these effects.

Two matrices are used when separate (smaller) Monte Carlo simulations are used:

- **Background Fluctuation Matrix**: used to remove background fluctuations, obtained from the MC simulations.
- **Detector Response Matrix**: used to remove detector effects. This matrix is obtained by comparing the results from the ”real” (MC simulated) jet p_T distribution to the obtained (MC simulated) jet p_T distributions with detector effects.

These matrices are combined into one matrix, when a full MC simulation is run.

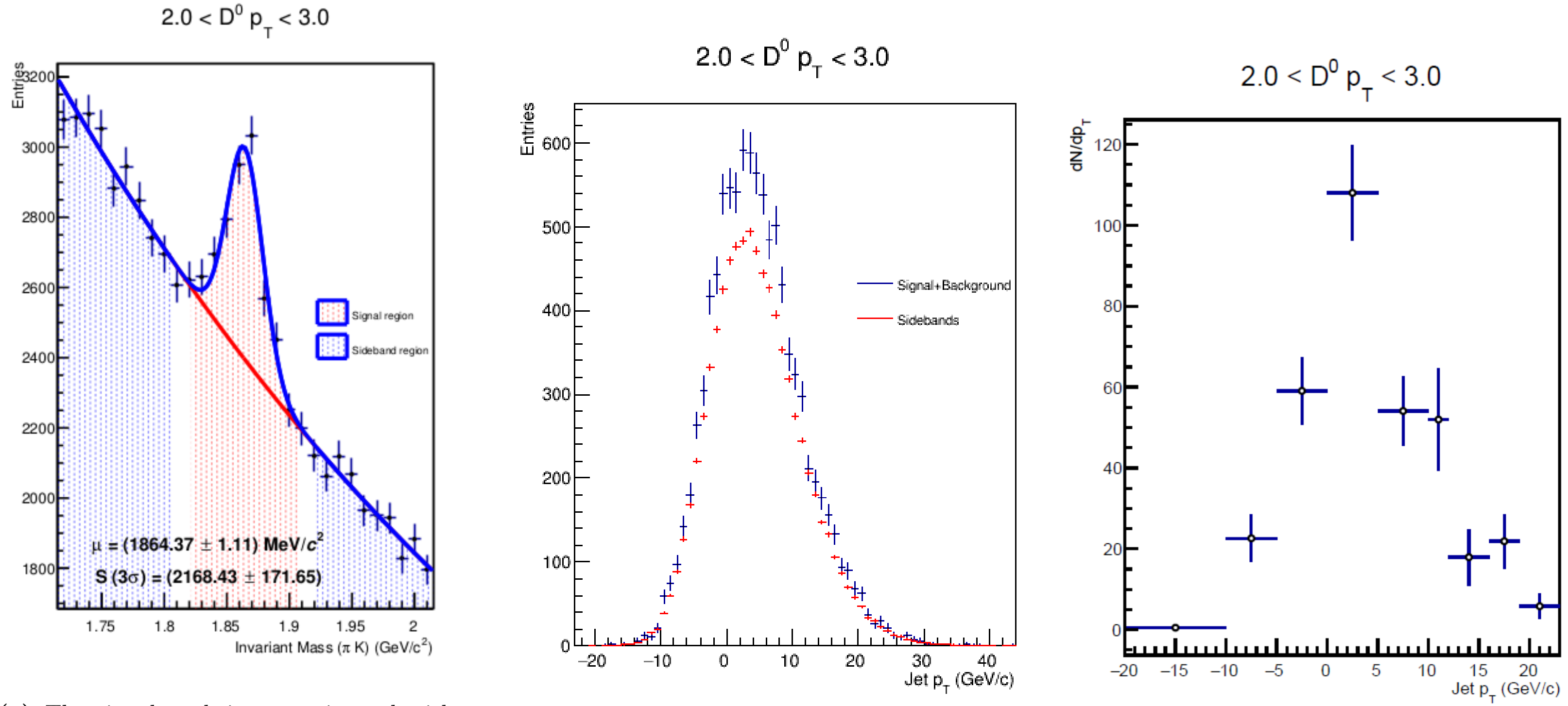

(a) The signal peak is approximated with a gaussian. The [signal with background] region is red-coloured and has a width of 3 sigma around the mean. The [sideband] regions are coloured in blue. They are *outside* the range of 4 sigma around the mean.

(b) The yield for [signal with background] (red area in figure 3.8a) is shown in blue. The yield for the [rescaled sideband] region (blue area in figure 3.8a) is shown in red.

(c) This figure shows the jet p_T spectrum of one D^0 p_T bin. This is obtained by subtracting the yield of the [sideband] region from the yield of the [signal with background] region. This [signal] yield is then corrected for bin width (dN/dp_T).

Figure 3.8 – Illustration of the three steps in the orange procedure, done for one D^0 p_T bin: $[2, 3)$ GeV/c.

Chapter 4

Results

In the following two sections, the results are presented for the purple and orange procedure. This is done for the central selection cut set only. The exact same two procedures were followed for the looser, tighter and AR selection cut sets. These resuls can be found in Appendix B.

Jet spectra for all selection cut sets are further studied in Chapter 5.

4.1 Purple Procedure

The purple procedure (as described in section 3.6.1) is defined to use the following ranges: jet p_T $[-20, 23)$ GeV/c and D^0 p_T $[2, 12)$ GeV/c. The distributions are also corrected for the efficiency caused by selection cuts and detector resolution.

The purple procedure was also done without efficiency correction. In this case, the procedure described in section 3.6.1 was followed, but no corrections for efficiency were done.

4.1.1 Invariant Mass of D^0-meson

The invariant mass distributions were obtained by projecting the D^0 p_T axis and jet p_T bin to the $(K\pi)$ pair invariant mass axis. A fit was done using a gaussian to fit the signal peak and an exponential function to fit the background.

The invariant mass distributions obtained from the purple procedure without efficiency correction is shown in figure 4.2a. The fit for bin $[-20, -10)$ GeV/c failed.

The distribution for the purple procedure with correction is shown in figure 4.2b. The result for bin $[12, 16)$ GeV/c does not have the expected sharper peak, it is a very broad, low peak. In figure 4.2a, the peak in this bin has the expected shape. Therefore, the separate D^0 p_T bins were studied for for all jet p_T bins. Figure 4.1 shows the separate D^0 p_T bins for jet p_T bin $[12, 16)$ GeV/c. It shows that the content in bin $[2, 3)$ GeV/c is mostly fluctuations rather than signal (which would be a well-defined mass peak). The same is true for the higher jet p_T bins. Thus, the invariant mass distributions can be improved by cutting D^0 p_T bin $[2, 3)$ GeV/c for jet p_T bins ≥ 12 GeV/c.

The same cut is done for jet p_T bin $[10, 12)$ GeV/c. However, this is based on the jet p_T distributions discussed in section 5.2.

Therefore, an extra cut was done: D^0 p_T bin $[2, 3)$ GeV/c is cut for jet p_T bins ≥ 10 GeV/c. The results for the purple procedure without efficiency correction can be found in figure 4.2c. There is no clear improvement of the distributions after the cut, seen in figure 4.2c, compared to distributions before the cut, seen in figure 4.2a.

The distributions for the purple procedure with efficiency correction and extra D^0 p_T cut shown in figure 4.2d, show the improvement for the jet p_T bins 10 GeV/c and higher compared to figure 4.2b.

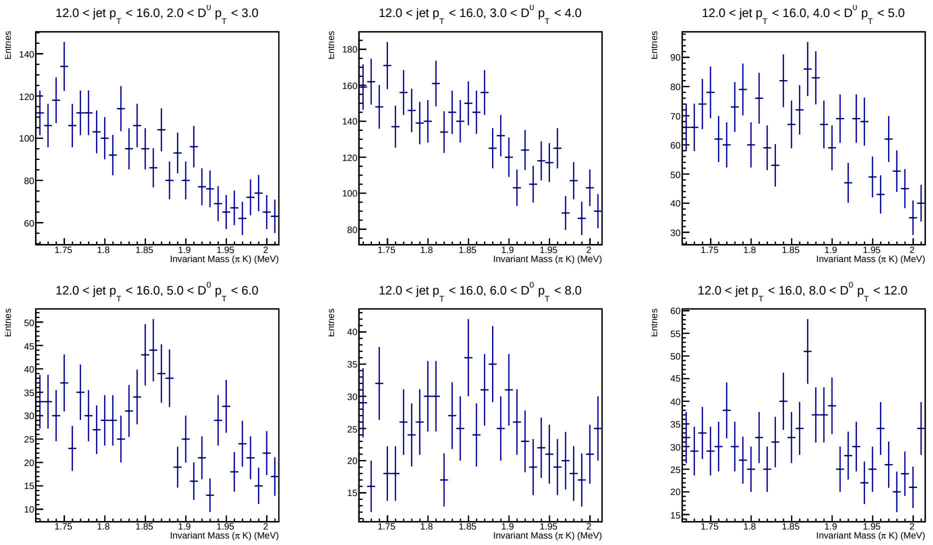

Figure 4.1 – Invariant mass spectra for separate D^0 p_T bins of jet p_T bin $[12, 16)$ GeV. Bin $[2, 3)$ GeV/c contains background and little signal.

4.1.2 Parameters

Parameters can be extracted from the fit done in section 4.1.1. The mean mass of D^0, sigma, signal over background ratio (s/b ratio) and the jet p_T spectrum can be found in figure 4.3a, presented in jet p_T bins. The parameters from the fits on the invariant mass distributions without efficiency corrections are shown in blue; the parameters taken from the fit on the distributions with efficiency correction are shown in red. The final jet p_T distribution is also shown: this is the signal yield corrected for the bin width.

Bin $[-20, -10)$ GeV/c has a very low mass and sigma compared to the other bins. The invariant mass distributions without efficiency correction (figures 4.2a and (figures 4.2c) demonstrate how little entries this bin actually has. Also, the s/b ratio is very high, meaning that signal should be very clear: however, this is not true for those figures. Therefore, this bin has been removed in the final jet p_T distributions.

For the higher jet p_T bins ($\geq$ 10 GeV/c) in figure 4.3a, sigma and the s/b ratio fluctuate a lot. This further adds to the suspicion that fluctuations play a bigger role in these bins. This is confirmed by figure 4.3b, which shows the parameters for the purple procedure with D^0 p_T bin $[2, 3)$ GeV/c cut out for jet $p_T \geq 10$ GeV/c. Here, these parameters are more stable and in accordance with the parameters in the case without efficiency correction.

The mass of the D^0-meson is (1864 ± 0.05) MeV/c^2 [16]. This mass value is within range of error in the case of the purple procedure without efficiency correction with and without the extra D^0 p_T cut. In case of the purple procedure, corrected for efficiency, its extracted mass values are close. However, due to the unrealistic small errors, no good conclusion can be drawn.

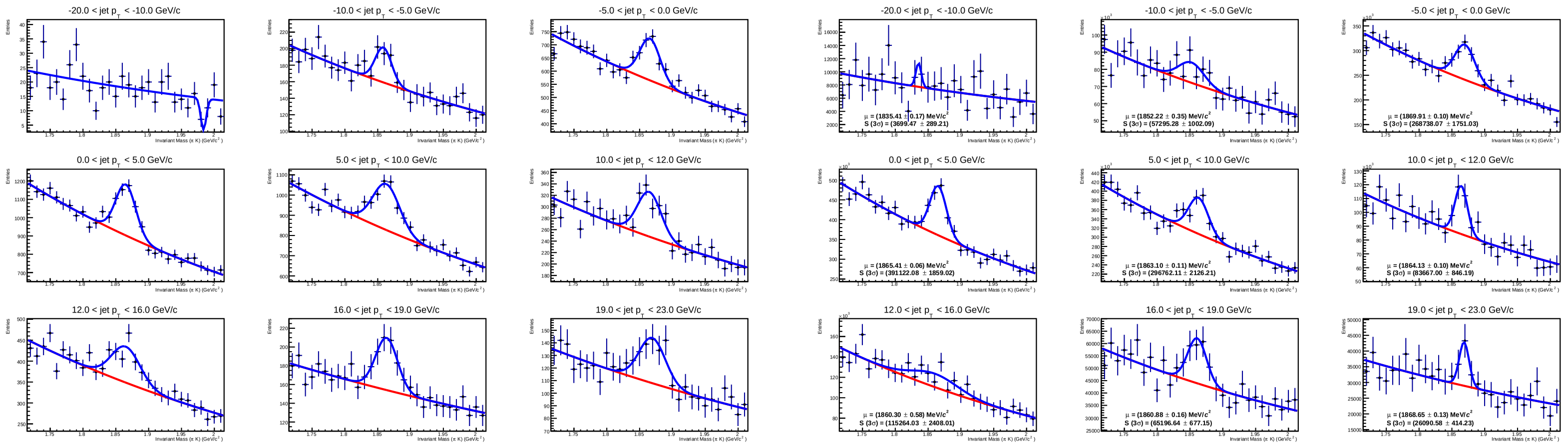

(a) Invariant mass distributions of the purple procedure with *no* correction for efficiency. The fit in bin $[-20, -10)$ GeV/c failed.

(b) Invariant mass distributions of the purple procedure *with* correction for efficiency. The peak in bin $[12, 16)$ GeV/c is unexpectedly flat and broad.

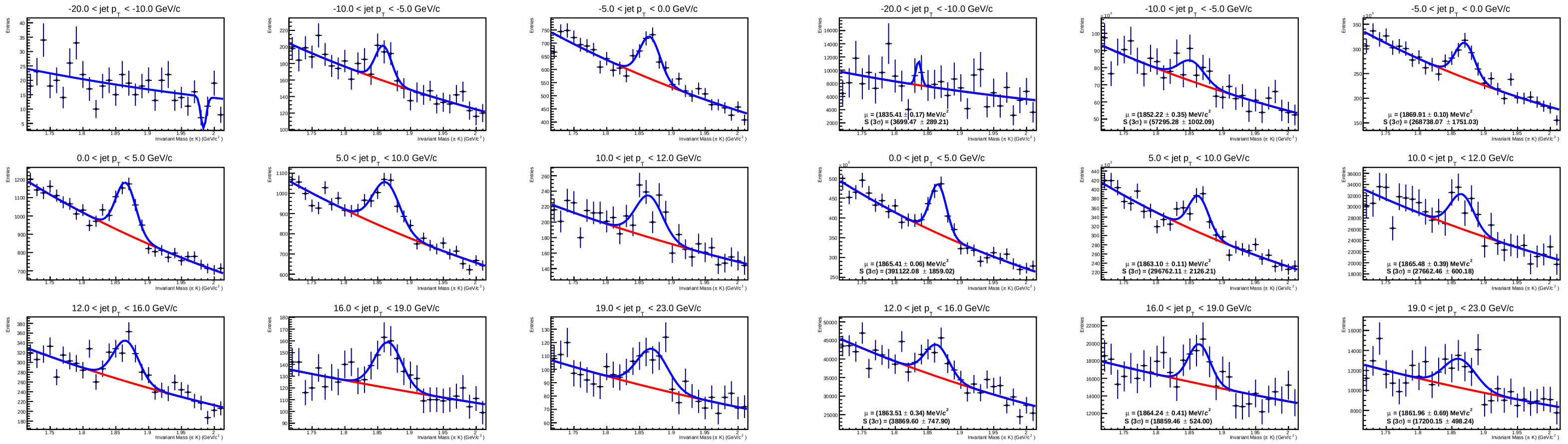

(c) Invariant mass distributions of the purple procedure with *no* correction for efficiency. For jet $p_T \geq 10$ GeV/c, D^0 $p_T \geq 3$ GeV/c.

(d) Invariant mass distributions of the purple procedure *with* correction for efficiency. For jet $p_T \geq 10$ GeV/c, D^0 $p_T \geq 3$ GeV/c.

Figure 4.2 – Invariant mass distributions from the purple procedure; without and with efficiency correction; without and with extra D^0 p_T cut.

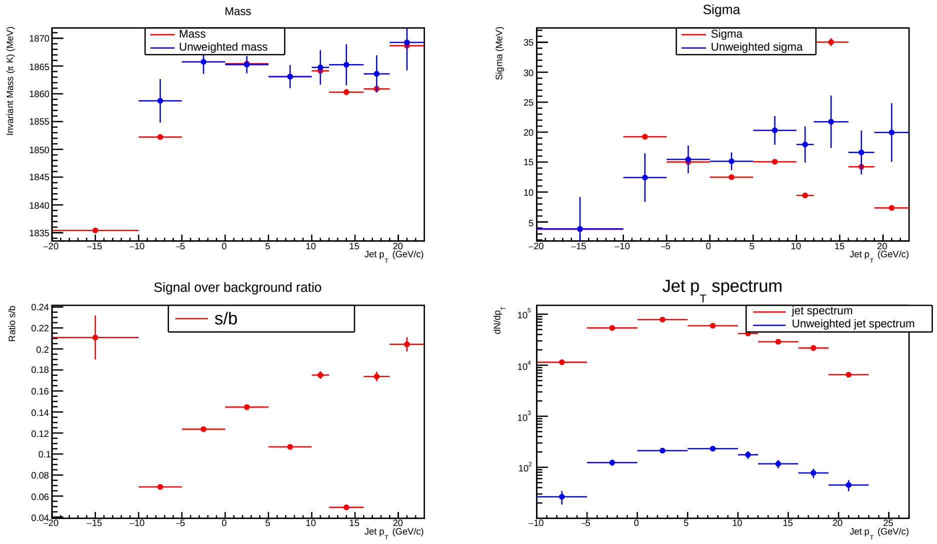

(a) Parameters extracted from the invariant mass distributions from purple procedure.

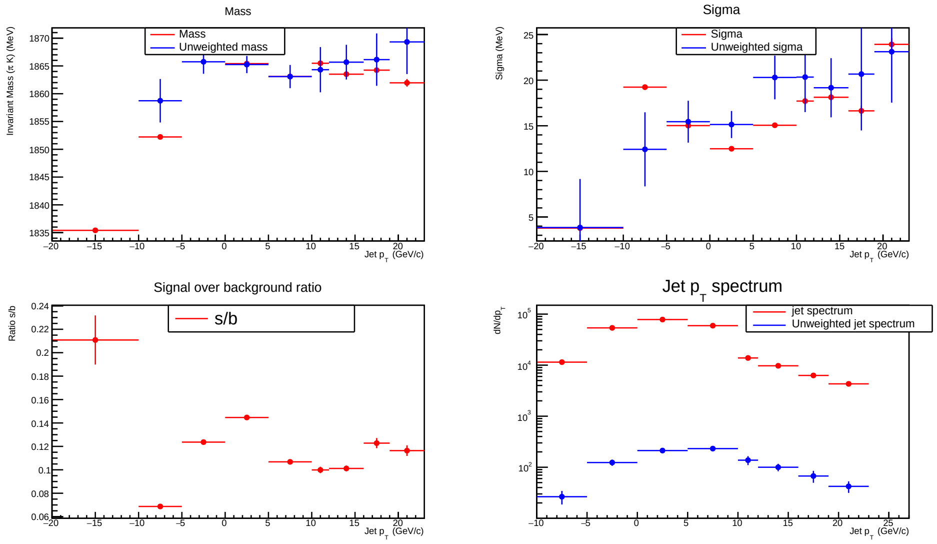

(b) Parameters extracted from the invariant mass distributions from the purple procedure. Here, for jet $p_T \geq 10$ GeV/c, D^0 $p_T \geq 3$ GeV/c.

Figure 4.3 – In blue, the parameters from the distributions without efficiency correction. The parameters from the distributions with efficiency correction are shown in red.

4.2 Orange Procedure

The orange procedure (as described in section 3.6.2) is defined to use the following ranges: jet p_T $[-20, 23)$ GeV/c and D^0 p_T $[2, 12)$ GeV/c. The distributions are also corrected for the efficiency.

The orange procedure was can also be done without efficiency correction. The procedure described in section 3.6.2 was followed without correcting for efficiency. This only affects the final jet p_T distribution, as in the steps before this, there is no correction for efficiency done yet.

4.2.1 Invariant Mass of D^0-meson

The invariant mass distributions obtained from the orange procedure is shown in figure 4.4. They are obtained by projecting the D^0 p_T bin and jet p_T axis to the $(K\pi)$ pair invariant mass axis. Similar to the purple procedure, signal is fitted with a guassian and background with an exponential function. The [signal] region is indicated in red; the [sideband] region is indicated in blue. The signal peaks are well-defined.

Note that the distributions are the same for the orange procedure with and without efficiency correction: the efficiency correction is only done when summing up the presented histograms.

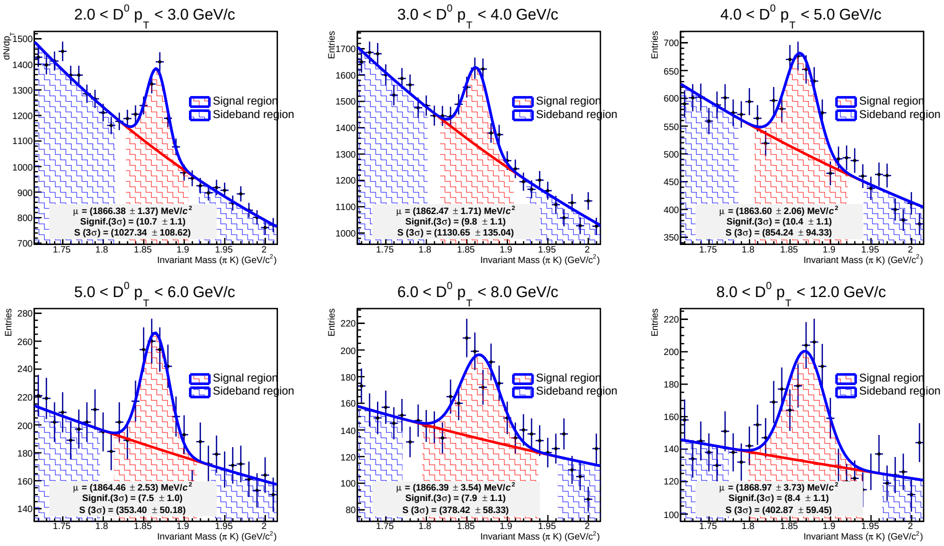

Figure 4.4 – The invariant mass distributions from the orange procedure. Note that none of these are corrected for efficiency: this only happens when summing these histograms up. The [signal] region is indicated in red. The [sideband] region is shown in blue.

4.2.2 Jet Spectrum

The jet p_T distribution, shown in figure 4.6a, was obtained by subtracting the yield from the [rescaled sideband] regions from the [signal with background] regions (indicated in figure 4.4). These results are also corrected for bin width. Again, these distributions are the same for the orange procedure with and without efficiency correction.

All bins have the a clear peak around 0 except for bin $[8, 12)$ GeV.

In the purple procedure, an extra cut was done: D^0 p_T $[2, 3)$ GeV/c was removed for jet $p_T \geq 10$ GeV/c. This cut can also be applied in the orange procedure. The only difference with figure 4.6a is that the contibutions of jet p_T bins $[10, 23)$ GeV/c of D^0 p_T bin $[2, 3)$ GeV/c are removed. This has no further impact on invariant mass, only on the final jet p_T distribution.

The final jet p_T distributions for four versions of the orange procedure are shown in figure 4.6b. The jet p_T distribution from the orange procedure without efficiency correction is shown in black. The distribution shown in green is from the orange procedure without efficiency correction where D^0 $p_T \geq 3$ GeV/c for jet $p_T \geq 10$ GeV/c. The distributions shown in blue and purple are from the orange procedure corrected for efficiency, without and with the same D^0 p_T cut, respectively. Note that the entries for the range $[-10, 10)$ GeV/c are the same for the procedures with and without extra D^0 p_T cut.

4.2.3 Parameters

Parameters have been extracted from the fit done in section 4.2.1. The mean mass (of D^0), sigma, signal over background ratio (s/b ratio) can be found in figure 4.5. These are presented in D^0 p_T binning. The jet p_T distribution shown in figure 4.5 is from the orange procedure, corrected for efficiency.

The mean mass, sigma and s/b ratio increase as D^0 p_T increases. This is expected, since the detector resolution of the ALICE subsystems is less precise at higher momenta. The significance in all D^0 p_T bins are above 3 sigma, meaning that the gaussian mass peaks in the invariant mass distributions (see figure 4.4) are relevant and not simple chance.

The experimental value of D^0 mass (1864 ± 0.05) MeV/c^2 [16]) is within range of error of most D^0 p_T bins.

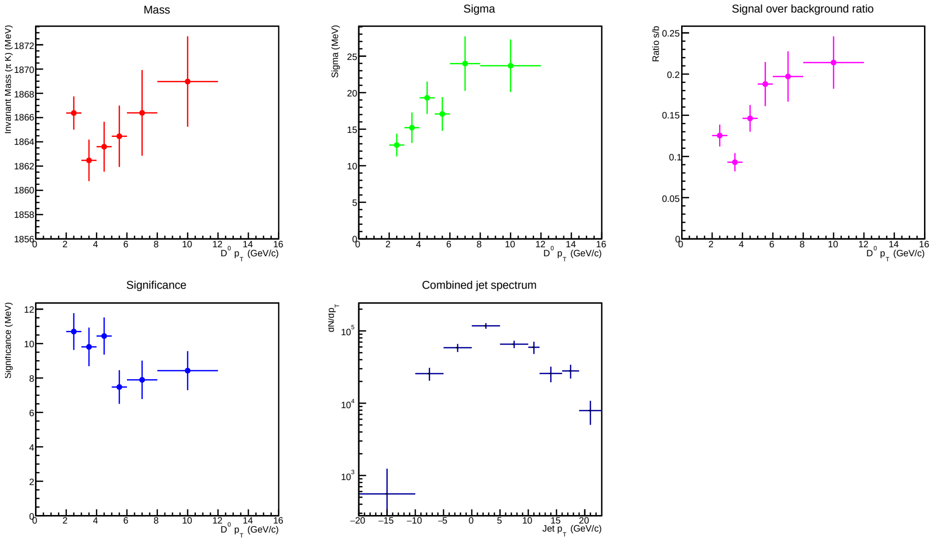

Figure 4.5 – Parameters from the orange procedure. Since these are taken straight from the invariant mass distributions per D^0 p_T bin, they are not corrected for efficiency. The jet spectrum is corrected for efficiency and shown in jet p_T bins.

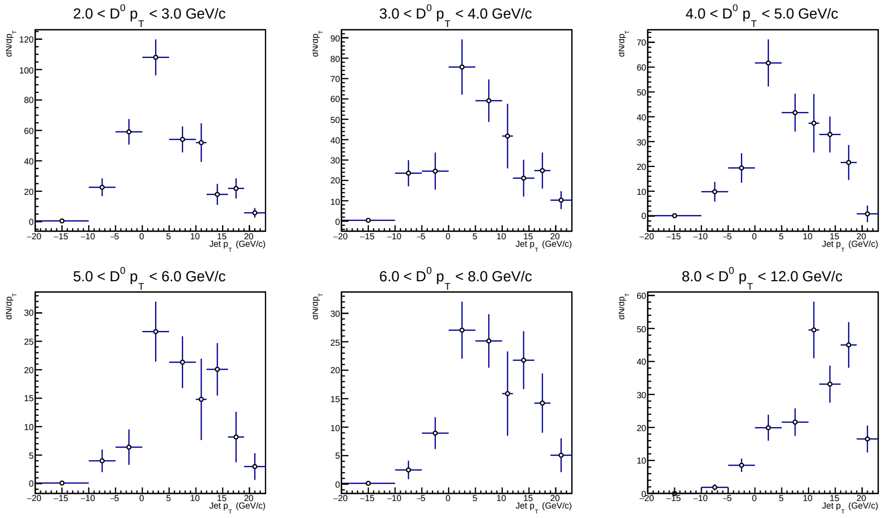

(a) The jet p_T distributions from the orange procedure. Note that these are not corrected for efficiency: this is only done when summing these distributions up. The D^0 p_T cut applied in the purple procedure can also be done in the orange procedure: the contributions of jet $p_T \geq 10$ GeV/c in D^0 p_T bin $[2, 3)$ GeV/c are removed.

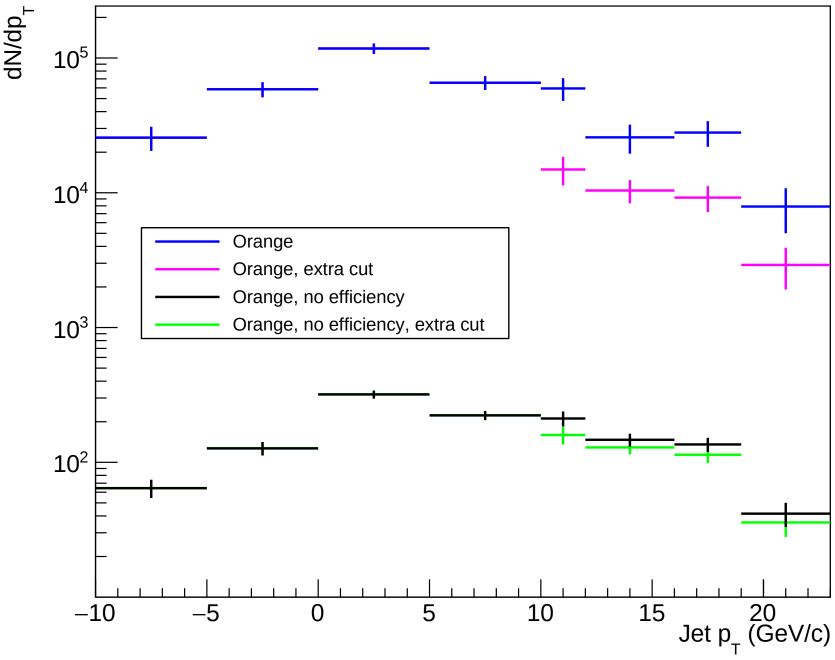

(b) The jet p_T distributions from the orange procedure. The distributions corrected for efficiency are shown in blue and purple; the distribution shown in purple is for the additional D^0 p_T cut. The distributions without efficiency correction are shown in black and green. The distribution shown in green also has the extra D^0 p_T cut.

Figure 4.6 – Jet p_T distributions in the orange procedure.

Chapter 5

Discussion

5.1 Discussing the Results

For the purple procedure with efficiency correction, the errors of the parameters and jet spectrum (for instance in figure 4.3) are very small. The fit on the invariant mass distribution determines the value of the error. Scaling the histogram after this fit does not influence the size of the error relative to the yield. However, it may be caused by scaling the separate D^0 p_T bins of invariant mass with 1/efficiency and then add them up. This is not the real distribution of invariant mass, which could lead to unrealistic errors.

The parameters for the purple procedure *without* efficiency correction have more realistic errors.

The orange procedure has more stable results: in principle, no additional cuts are needed to improve invariant mass distributions and the parameters behave as expected.

The big difference between the orange and purple procedure is of course the moment of correction for efficiency. In purple, if there are fluctuations, especially in the lower D^0 p_T bins[1], they get amplified and therefore play a bigger role. Therefore, an additional D^0 p_T cut was done in section 4.1 to remove fluctuations that distorted the invariant mass distributions and extracted paramters: for jet $p_T \geq 10$ GeV/c, D^0 $p_T \geq 3$ GeV/c rather than 2 GeV/c.

This is not the case for the orange procedure, where the correction for background and fluctuations is done before the efficiency correction. However, in order to compare the orange and purple procedure, the orange procedure was also carried out with this additional D^0 p_T cut.

5.2 Comparing Jet Momentum Spectra

For both the purple and orange procedure there are the following versions of the procedures:

- Procedure without efficiency correction.
- Procedure without efficiency correction, where D^0 $p_T \geq 3$ GeV/c for jet $p_T \geq 10$ GeV/c.
- Procedure with efficiency correction.
- Procedure with efficiency correction, where D^0 $p_T \geq 3$ GeV/c for jet $p_T \geq 10$ GeV/c.

In this section, the obtained results will be compared in order to determine the behaviour of the jet p_T distributions under different selection cuts and the two procedures.

---

[1] See figure 3.4: the efficiency in lower D^0 p_T bins is small, therefore the scaling factor 1/efficiency is very large.

The purple and orange procedure are compared for four different selection cut sets: central (these results were shown in Chapter 4), looser, tighter and AR. This comparison is done to determine how much influence the choice of selection cuts has on the jet p_T distribution. Ideally, the resulting distributions (with efficiency correction and additional cuts) are the same. However, the distributions may differ due to systematic uncertainties of the analysis. Note that the distributions without these corrections are *not* expected to be the same.

The procedures with and without efficiency correction are also compared in order to determine the stability of the procedure when there is a correction for efficiency done. As mentioned in section 5.1, the correction seems to play a bigger role in the purple procedure than in the orange procedure. In this section, it is shown that this can also be seen in the jet p_T distributions.

In the following figures, all distributions are corrected for the number of selected events. These numbers are given in table 5.1. They do not differ much: the biggest relative difference is 1.2%. Note that both the looser and tighter selection cut sets have a lower number of selected events than the central set. This is expected: the central selection cuts are "optimal" cuts, meaning that the looser and tighter selection cuts are less than "optimal". This results in a lower number of selected events. Next to that, the looser selection cuts have fewer events than the tighter set. This is unexpected, since the looser selection cuts and its efficiency (shown in green in figure 3.4) indicate that more events would be selected, compared to the tighter cuts.

Set of cuts	**Number of selected events**
Central	7368460
Looser	7331750
Tighter	7356340
AR	7420830

Table 5.1 – Overview of the number of selected events per dataset.

Next to that, the jet p_T bin $[-20, -10)$ GeV/c has been removed from all distributions. There were very few entries in this bin and fluctuations have a bigger influence than in higher jet p_T bins. This is especially true for the purple procedure.

Figure 5.2 shows all the jet p_T distributions from the purple procedure for all four selection cut sets.

The distributions without efficiency correcion, shown in figure 5.2a, mostly have similar shapes. Due to the values of the selection cuts, it is expected that the distribution for the central cuts to be below the looser set and above the tighter set. The central selection cuts are more closed than the looser selection cuts. This result in a lower yield for the central selection cuts. The central selection cuts are less closed than the tighter selection cuts. This results in a higher yield compared to the tighter selection cuts. This is indeed true for all jet p_T bins.

When D^0 p_T bin $[2, 3)$ GeV/c is removed for jet $p_T \geq 10$ GeV/c, this still holds for all bins except jet p_T bin $[12, 16)$ GeV/c, which can be seen in figure 5.2b.

The jet p_T distributions from the purple procedure with efficiency correction are shown in figure 5.2c. The entry from the looser set in bin $[-10, -5)$ GeV/c deviates from the other entries in that bin. However, the invariant mass distribution (which can be found in Appendix B) show a very flat, broad peak: clearly this is not a correct result. Therefore, the entry from the looser set in bin $[-10, -5)$ GeV/c can be ignored.

Up to jet p_T 10 GeV/c, the distributions have similar shapes and are close to each other. For jet $p_T \geq 10$ GeV/c, the distributions are widespread. In the bins $[12, 23)$ GeV/c, D^0 p_T bin $[2, 3)$ GeV/c was removed due to fluctuations in the invariant mass distributions. There was no such clue for jet p_T bin $[10, 12)$ GeV/c before, but this figure illustrates that there are fluctuations in this bin too. Therefore, the same D^0 p_T cut was done for bin $[10, 12)$ GeV/c too.

As seen in figure 5.2d, the distributions in this range after the additional D^0 p_T cut are closer to each other. The distribution of the central set is not always between the distributions of the looser and tighter set. In fact, the distribution of the looser set is the lowest entry in three of seven[2] bins. This would indicate the efficiency correction does not work as it should in the purple procedure, or that additional cuts need to be done.

It is expected that these fully corrected distributions in figure 5.2d are the same or consistent within range of error. But it is hard to judge whether this is true since the errors are unrealistically small. This is an important disadvantage of the purple procedure with efficiency correction.

Nonetheless, looking at the difference of the distributions from the AR, looser and tighter selection cut sets relative to the distribution from the central selection cut set can give an indication if the fully correction jet p_T distributions are consistent. Figure 5.1 shows the jet p_T distributions from figure 5.2d with the distribution from the central selection cut set subtracted from them. There is no symmetry between the deviations of the tighter and looser selection cut sets, which is expected since the looser and tighter selection cuts are about the same variation up and down, respectively, of the central selection cuts.

The major number of entries differ less than $1 \cdot 10^{-3}$ (GeV/c)$^{-1}$ compared to the entries from the jet p_T distribution of the central set. The maximum deviation is around $2 \cdot 10^{-3}$ (GeV/c)$^{-1}$.

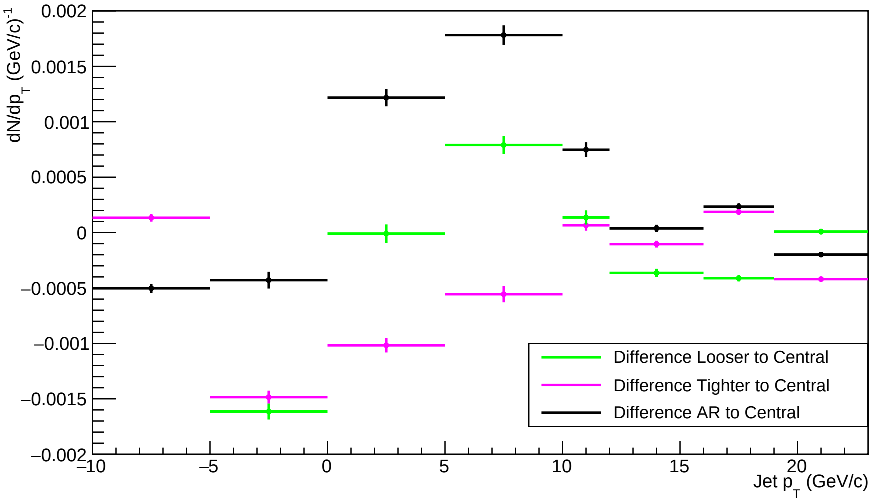

Figure 5.1 – Difference between the entries from the distributions from the corrected purple procedure for: the looser, tighter and AR selection cut set compared to the distribution from the central cut set. These are in green, pink and black, respectively. The fully corrected purple procedure is not consistent for different selection cuts. Most entries differ less than $1 \cdot 10^{-3}$ (GeV/c)$^{-1}$ from the entries of the central set. However, how much they differ highly depends on the jet p_T bin and selection cut set.

---

[2] Not considering jet p_T bin $[-10, -5)$ GeV/c.

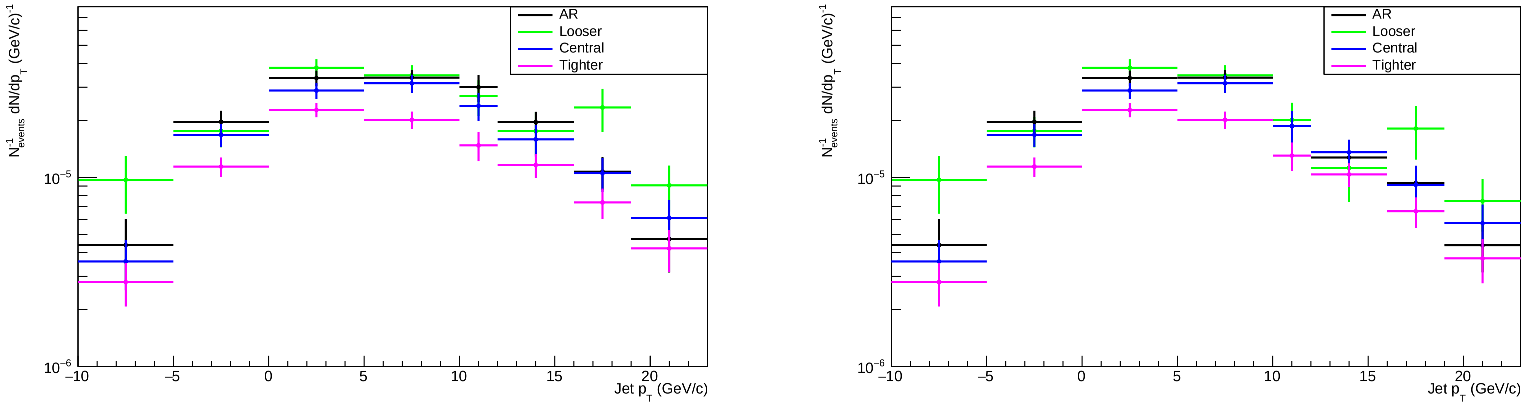

(a) Jet p_T distribution from the purple procedure without efficiency correction. Here, D^0 $p_T \geq 2$ GeV/c for all jet p_T.

(b) Jet p_T distribution from the purple procedure with D^0 $p_T \geq 3$ GeV/c for jet $p_T \geq 10$ GeV/c.

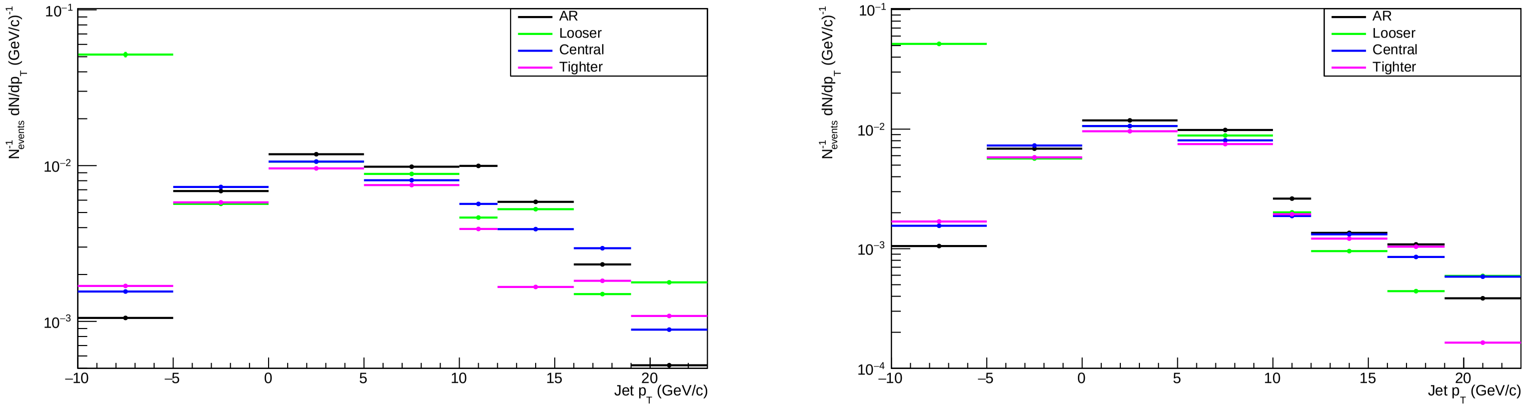

(c) Jet p_T distribution from the purple procedure. D^0 $p_T \geq 2$ GeV/c for all jet p_T.

(d) Jet p_T distribution from the purple procedure with D^0 $p_T \geq 3$ GeV/c for jet $p_T \geq 10$ GeV/c.

Figure 5.2 – Comparison of the jet p_T distribution from the purple procedure with and without efficiency correction and D^0 p_T cut. The results for AR are in black, looser in green, central in blue and tighter in pink.

All jet p_T distributions from the orange procedure for all four selection cut sets are shown in figure 5.4.

Figure 5.4a shows that, as expected, for all jet p_T bins the distribution of the central set is below the distribution of the looser set and above the tighter set. The same is true for the distributions in figure 5.4b, where D^0 p_T bin $[2, 3)$ GeV$/c$ contains no entries for jet $p_T \geq 10$ GeV$/c$. The distributions are not expected to be the same or consistent, and indeed they are not.

The jet p_T distributions from the orange procedure with efficiency correction are shown in figures 5.4c and 5.4d. The latter contains the distributions for the additional D^0 p_T cut. In both figures, again, the distributions from the central set are between the distributions from the looser and tighter sets for almost all bins. This indicates that the efficiency correction is (nearly) correct.

The fully corrected jet p_T distributions, shown in figure 5.4d, have similar shapes for the four sets. However, the distribution of the looser selection cut set is often out of range of error from distributions of the central set (and others). The distributions of AR and the tighter selections cut sets are almost always within range of error of the distribution of the central set.

Figure 5.3 presents the difference between the fully corrected jet p_T distributions from the AR, looser and tighter selection cut sets and the central selection cut set. The difference between the distributions from the central and AR sets is around 0. As expected, the deviation of the distribution of the looser and tighter sets from the central set is approximately mirrored: when the deviation of the tighter set is $-Y$, the deviation of the looser set is approximately $+2Y$.

The maximum difference is about $8 \cdot 10^{-3}$ (GeV$/c)^{-1}$. This is 3 times larger than the maximum difference in the fully corrected purple procedure. Most entries deviate by less than $2 \cdot 10^{-3}$ (GeV$/c)^{-1}$. This is the maximum deviation in the purple procedure.

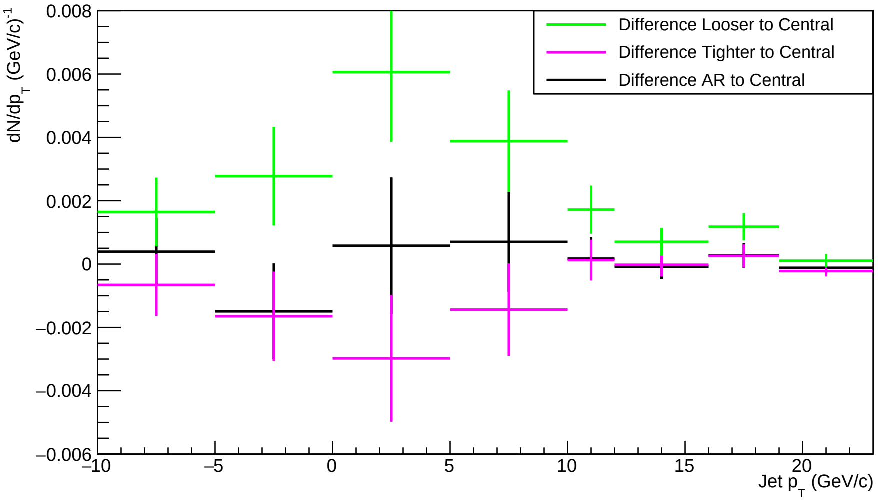

Figure 5.3 – Difference between the entries from the distributions from the corrected orange procedure for: the looser, tighter and AR selection cut set compared to the distribution from the central cut set. These are in green, pink and black, respectively. The fully corrected orange procedure is not consistent under different selection cuts. Most entries deviate by about $2 \cdot 10^{-3}$ (GeV$/c)^{-1}$. This is the maximum deviation in the fully corrected purple procedure.

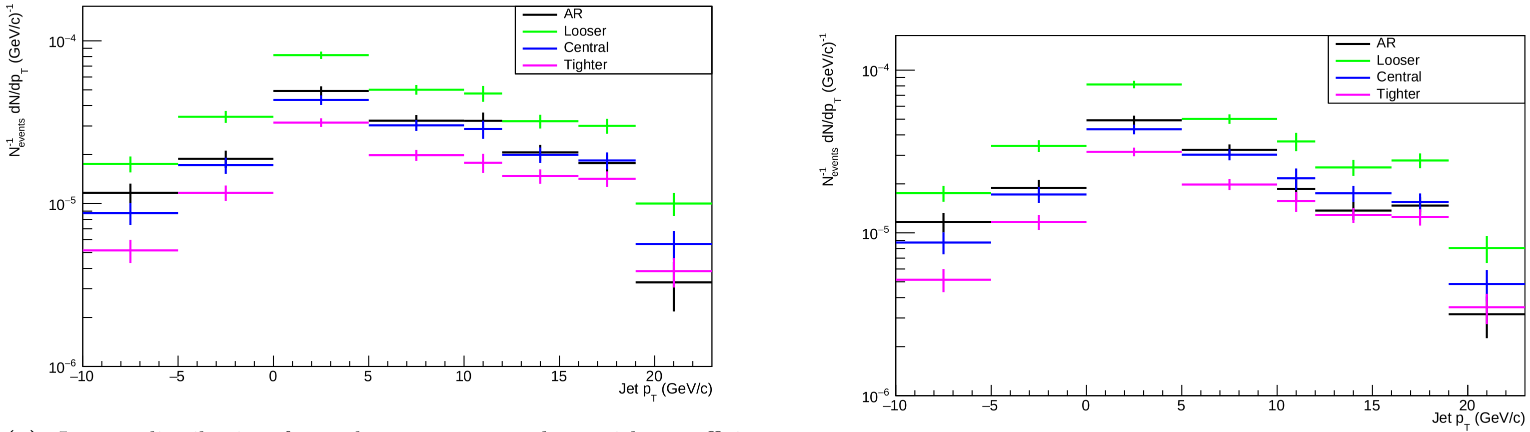

(a) Jet p_T distribution from the orange procedure without efficiency correction.

(b) Jet p_T distribution from the orange procedure without efficiency correction. For D^0 p_T bin $[2, 3)$ GeV/c, the contributions of jet $p_T \geq 10$ GeV/c have been removed.

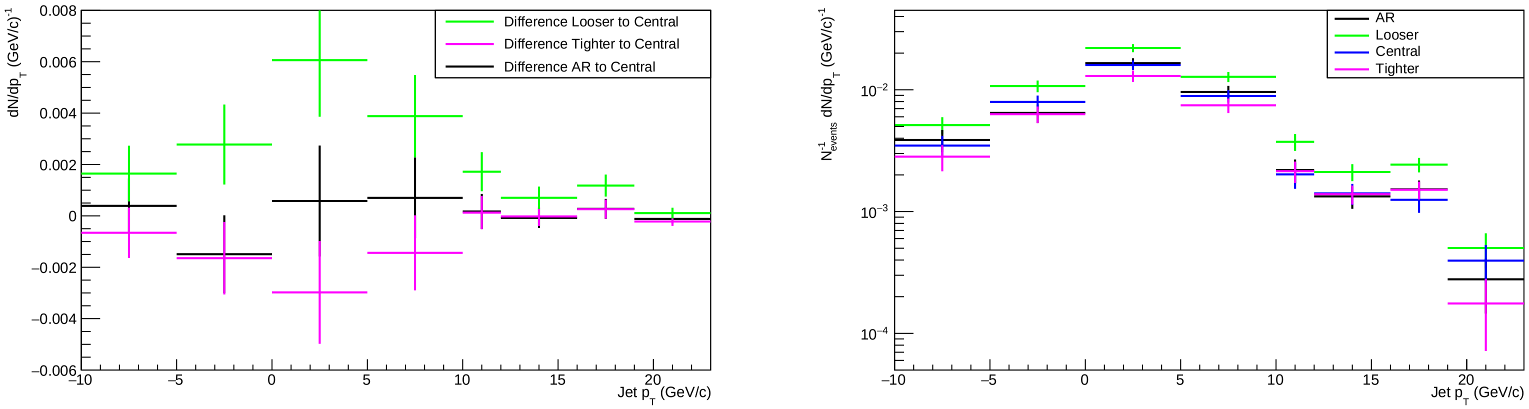

(c) Jet p_T distribution from the orange procedure, corrected for efficiency.

(d) Jet p_T distribution from the orange procedure, corrected for efficiency. For D^0 p_T bin $[2, 3)$ GeV/c, the contributions of jet $p_T \geq 10$ GeV/c have been removed.

Figure 5.4 – Comparison of the jet p_T distribution from the orange procedure with and without efficiency correction and D^0 p_T cut.

The purple and orange procedure with D^0 p_T bin $[2,3)$ GeV/c removed for jet p_T $\geq$ 10 GeV/c are compared per selection cut set in figure 5.6. The fully corrected jet p_T distributions from the purple and orange procedure are shown in dark blue and red, respectively. The distributions from the purple and orange procedure without efficiency correction are shown too, in light-blue and pink, respectively.

First consider the distributions from the procedures without efficiency correction. They are not expected to be the same, however for some bins they are within range of error. For the looser selection cut set (figure 5.6c), the entries are not within range of error but the shape of the distributions is very similar.

The fully corrected distributions are expected to be the same or consistent within range of error. Similar to the situation in figures 5.2c and 5.2d, this is difficult to determine due to the size of the errors of the distributions from the purple procedure. The difference between the jet p_T distributions from the fully corrected orange and purple procedure per set, shown in figure 5.5, can give an indication if the two procedures are consistent.

The corrected distributions from the looser set in figure 5.6c are not consistent, unless the errors in its corrected purple procedure distribution are much larger than the errors in the distribution of the corrected orange procedure.

The jet p_T distributions from the corrected purple and orange procedure from the central (figure 5.6a), tighter (figure 5.6d) and AR (figure 5.6b) selection cut set have consistent entries in the same five bins. This is also shown in figure 5.5: the difference between the two procedures is approximately 0.

This shows that the jet p_T distributions obtained with the fully corrected orange and purple procedure are *nearly* the same for the central, tighter and AR selection cut sets. The systematic uncertainty due to the method of analysis depends on the selection cut set and jet p_T bin, but is mostly no more than $2 \cdot 10^{-3}$ $(\mathrm{GeV}/c)^{-1}$.

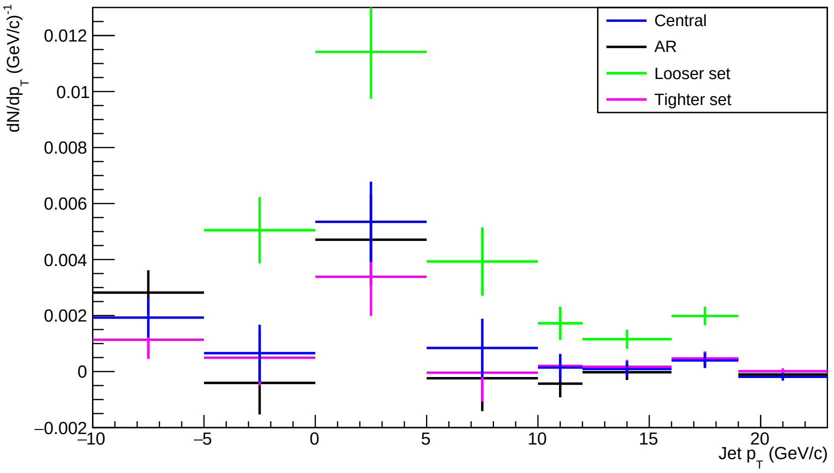

Figure 5.5 – Difference between the entries from the jet p_T distributions from the corrected purple and orange procedures. The central set is shown in blue; AR in black; looser in green and the tighter set in pink. The consistency of the two procedures depends on the selection cuts.

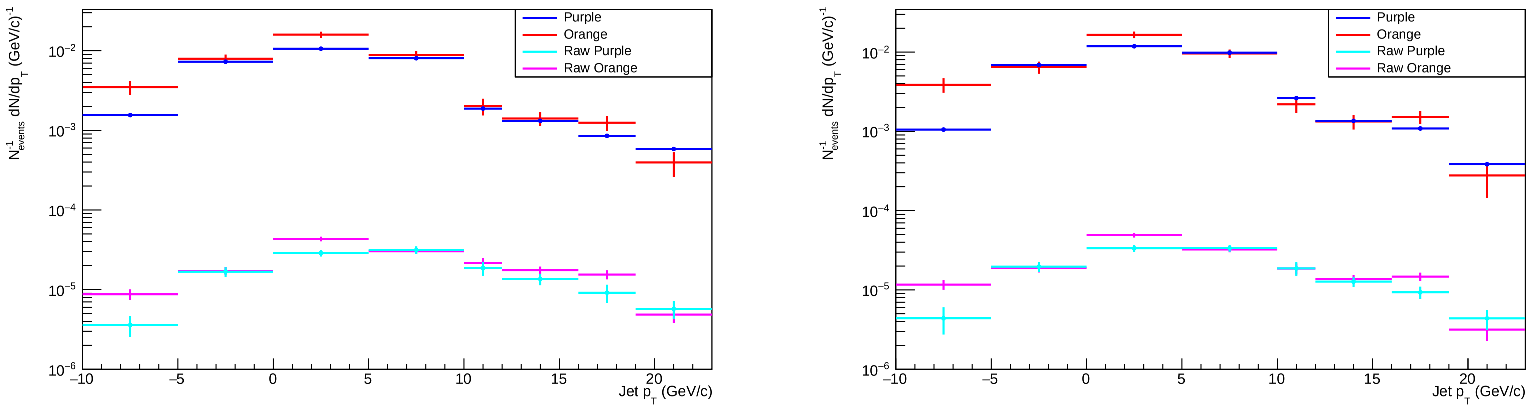

(a) Jet p_T distributions for the central selection cut set.

(b) Jet p_T distributions for the AR selection cut set.

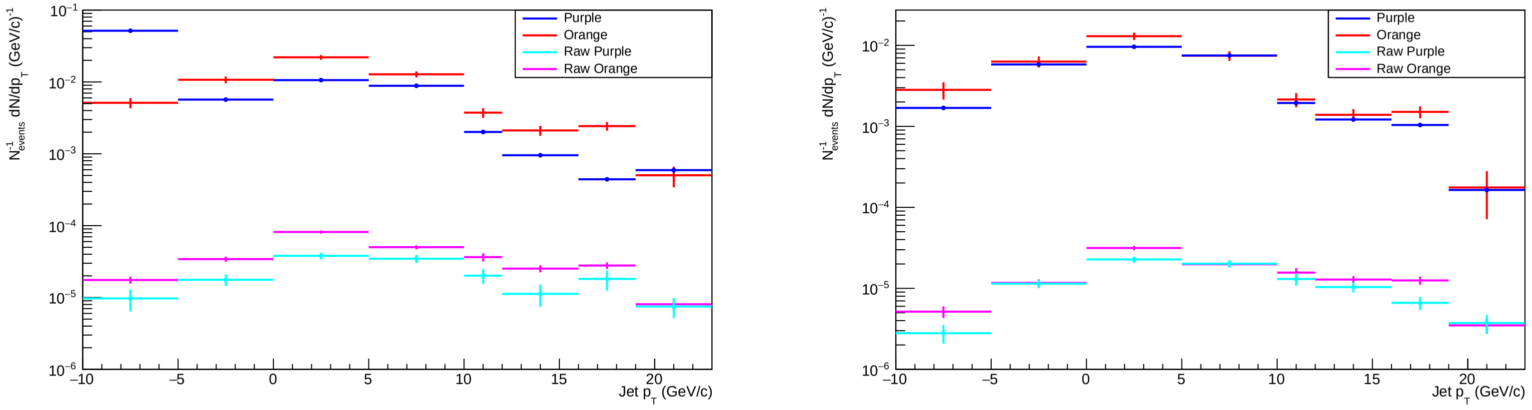

(c) Jet p_T distributions for the looser selection cut set.

(d) Jet p_T distributions for the tighter selection cut set.

Figure 5.6 – Comparing jet p_T distribtions per selection cut set. These are the distributions with additional D^0 p_T cut for jet pt$\geq$ 10 GeV/c. The distributions with efficiency correction are shown in pink and light blue. The distributions with efficiency correction are shown in red and dark blue.

Chapter 6

Conclusion and Outlook

The charm jet transverse momentum distribution is an important observable when it comes to charm production and studying the Quark-Gluon Plasma that may be produced in Pb-Pb collisions in ALICE. In this study, the systematic uncertainties in the obtained jet p_T distribution due to selection cuts and method of analysis have been investigated. This distribution was obtained from the invariant mass distribution of $(K\pi)$-pairs, D^0-meson transverse momentum and the transverse momentum of jets containing a D^0-meson.

The following conclusions can be drawn:

- The purple procedure with efficiency correction is very sensitive to fluctuations. The correct cuts in D^0 p_T have to be made in order to obtain a reasonable invariant mass distribution and consequently a reasonable jet p_T distribution. The errors in the parameters and jet p_T distribution resulting from the corrected purple procedure are unrealistically small. The shapes of jet p_T distributions for the four selection cut sets are not similar.

- The orange procedure with efficiency correction is not very sensitive to fluctuations, since corrections for background effects are done before correcting for efficiency. The shapes of the jet p_T distribution for the four selection cut sets are similar.

- In case of the purple procedure, correcting for efficiency does not lead to the expected configuration where the jet p_T distribution from the central selection cut set lies beneath the distribution from the looser selection cut set and above the distribution from the tighter selection cut set. On the contrary, this configuration is found in the orange procedure.

- The jet p_T distribution from the fully corrected purple and orange procedures are not consistent with itself for various selection cut sets. The systematic uncertainties are approximately $1 \cdot 10^{-3}$ and $2 \cdot 10^{-3}$ $(\mathrm{GeV}/c)^{-1}$, respectively.

- The fully corrected purple and orange procedure are not consistent with each other. They are *nearly* consistent for three out of four selection cut sets. Moreover, this confirms that the obtained jet p_T distribution depends on the selection cut set.

Especially the purple procedure as described in this thesis is not optimal yet for obtaining the jet transverse momentum distribution. This procedure can be improved by finding more favourable cuts to minimise the influence of background, fluctuations and absence of signal. It is also necessary to determine an approach that results in more realistic errors.

The orange procedure can be studied and optimised in an attempt to reduce the systematic uncertainy due to selection cuts.

The full analysis also includes unfolding the jet transverse momentum distribution. The results in this study were not unfolded. Hence, unfolding needs to be worked into the two procedures. In the purple procedure, this could be done when obtaining the final jet p_T distribution. In the orange procedure, the distributions per D^0 p_T bin could be unfolded before correcting for efficiency and adding them up. Another option would be unfold the final jet p_T distribution.

The comparison of the jet transverse momentum distribution for four selection cut sets and two procedures has resulted in an estimate of the systematic uncertainties of the analysis and at the same time demonstrated that there is room for improvement.

Bibliography

[1] ALICE, *Header: Heavy Ion Physics*, http://alipub.web.cern.ch/, may 18, 2016.

[2] E. M. Henley and A. Garcia, *Subatomic Physics* (World Scientific Publushing Co. Pte. Ltd., 57 Shelton Street, Covent Garden, London WC2H 9HE, 2007), 3rd ed., ISBN ISBN-10 981-270-056-0.

[3] Wikipedia, *Atomism*, https://en.wikipedia.org/wiki/Atomism, read at 3 May 2016.

[4] D. Griffiths, *Introduction to elementary particles* (John Wiley & Sons, 2008).

[5] Wikipedia, *Standard Model*, https://en.wikipedia.org/wiki/Standard_Model, read at 29 April 2016.

[6] G. Aad, T. Abajyan, B. Abbott, J. Abdallah, S. A. Khalek, A. Abdelalim, O. Abdinov, R. Aben, B. Abi, M. Abolins, et al., Physics Letters B **716**, 1 (2012).

[7] G. Bellini, I. I. Bigi, and P. J. Dornan, Physics Reports **289**, 1 (1997).

[8] M. R. Francis, Symmetry Magazine (2015), http://www.symmetrymagazine.org/article/do-protons-decay.

[9] L. Hesla, Symmetry Magazine (2016), http://www.symmetrymagazine.org/article/fermilab-scientists-discover-new-four-flavor-particle.

[10] J. Barth, W. Braun, J. Ernst, K.-H. Glander, J. Hannappel, N. Jöpen, H. Kalinowsky, F. Klein, E. Klempt, R. Lawall, et al., Physics Letters B **572**, 127 (2003).

[11] R. Aaij, B. Adeva, M. Adinolfi, A. Affolder, Z. Ajaltouni, S. Akar, J. Albrecht, F. Alessio, M. Alexander, S. Ali, et al., Physical review letters **115**, 072001 (2015).

[12] G. S. S. Bethke, G. Dissertori, *Quantum Chromodynamics*, Particle Data Group, http://pdg.lbl.gov/ (Revised in 2015).

[13] M. N. Chernodub, arXiv preprint arXiv:1001.0570 (2010).

[14] E. Norrbin and T. Sjöstrand, The European Physical Journal C-Particles and Fields **17**, 137 (2000).

[15] A.C. Oliveira da Silva and Suaide, A. A. P. and Mischke, A. (2015).

[16] C. Amsler et al., D^0, Particle Data Group, http://pdg.lbl.gov/2008/listings/s032.pdf (2008).

[17] J. Adams, M. Aggarwal, Z. Ahammed, J. Amonett, B. Anderson, D. Arkhipkin, G. Averichev, S. Badyal, Y. Bai, J. Balewski, et al., Nuclear Physics A **757**, 102 (2005).

[18] M. Nahrgang, J. Aichelin, S. Bass, P. B. Gossiaux, and K. Werner, Nuclear Physics A **931**, 575 (2014).

[19] A. Majumder and M. Van Leeuwen, Progress in particle and nuclear physics **66**, 41 (2011).

[20] CERN, *About CERN*, `http://home.cern/about`, read at 29 April 2016.

[21] CERN, *Large Hadron Collider*, `http://home.cern/topics/large-hadron-collider`, read at 3 May 2016.

[22] CERN, *CERN Document Server*, `http://cds.cern.ch/record/1436153`, found on May 23, 2016.

[23] ALICE Collaboration, International Journal of Modern Physics A pp. 51–66 (2014).

[24] A. Rossi, private communication.

[25] G. S. Matteo Cacciari, Gavin Salam, *FASTJET*, `http://fastjet.fr/`.

[26] M. Cacciari, G. P. Salam, and G. Soyez, Journal of High Energy Physics **2008**, 063 (2008).

Acknowledgements

The road to this thesis has been a five month long lesson. I started out with hardly any knowledge about programming. My understanding of the world of particle physics was basic. Thanks to the path to writing this thesis, I feel I now know more about both topics.

This thesis would not have been possible without my supervisor Barbara. Thank you for you guidance and patience throughout this journey and for solving problems with my code. Also, I want to thank Antonio for his helping hand. I would like to thank dr. André Mischke for his supervision and for giving me the opportunity to be a part of the QGP-ALICE research group. It has been great to see how this team interacts and cooperates.

To all the other students writing their thesis at SAP: thank you for the chatter and the support. Special thanks to Laurens for his very informative LaTeX course and his wonderful lay-out that I have adopted.

I would like to acknowledge friends and family for their support. I owe my gratitude to my mum, dad and Ilse for providing feedback, even though they knew next to nothing about this topic. Many thanks to my (very mathematical) friends Babette, Bjarne, Esther and Ruud for the friendship and shared journey these three years. Last but not least, I want to thank Rien for always being able to bring a smile on my face no matter how the coding that day had gone.

Appendix A: Selection cuts

Tables 1, 2 and 3 list the selection cuts on D^0 and its daughters (pion and kaon) for the 10% most central events for the looser and tighter cuts and Andrea Rossi's cuts, respectively.

The tighter cuts have the following changes with respect to the central cuts:

- $DCA_{tighter} = DCA_{normal} - 0.010$
- $(d_0^k d_0^\pi)_{tighter} = (d_0^k d_0^\pi)_{normal} + 15\%(d_0^k d_0^\pi)_{normal}$
- $|\cos(\theta_{point})|_{XY,\,tighter} = |\cos(\theta_{point})|_{XY,\,normal} + 0.05$
- If $|\cos(\theta_{point})|_{XY,\,tighter} > 0.98$, then set $|\cos(\theta_{point})|_{XY,\,tighter} = 0.98$

The looser cuts have the following changes with respect to the central cuts:

- $DCA_{looser} = DCA_{normal} + 0.015$
- $(d_0^k d_0^\pi)_{looser} = (d_0^k d_0^\pi)_{normal} - 15\%(d_0^k d_0^\pi)_{normal}$
- $|\cos(\theta_{point})|_{XY,\,looser} = |\cos(\theta_{point})|_{XY,\,normal} - 0.05$

D^0 p_T (GeV/c)	2-3	3-4	4-5	5-6	6-8	8-12	12-16	16-20	20-24	24-∞
Δm_{D_0} (GeV/c^2)	0.400	0.400	0.400	0.400	0.400	0.400	0.400	0.400	0.400	0.400
DCA (cm)	0.0400	0.0400	0.0400	0.0400	0.0450	0.0500	0.0550	0.0550	0.0550	0.0550
$\cos(\theta^*)$	0.8	0.8	0.8	0.8	0.8	1.0	1.0	1.0	1.0	1.0
K p_T (GeV/c)	0.7	0.7	0.7	0.7	0.7	0.7	0.7	0.7	0.7	0.7
π p_T (GeV/c)	0.7	0.7	0.7	0.7	0.7	0.7	0.7	0.7	0.7	0.7
$\|d_0^K\|$ (cm)	1.000	1.000	1.000	1.000	1.000	1.000	1.000	1.000	1.000	1.000
$\|d_0^\pi\|$ (cm)	1.000	1.000	1.000	1.000	1.000	1.000	1.000	1.000	1.000	1.000
$d_0^k d_0^\pi$ (10^{-4} cm^2)	3.8250	3.0600	2.2950	1.7850	1.1900	0.4250	0.0850	0.0850	0.0850	0.0850
$\cos(\theta_{point})$	0.90	0.90	0.90	0.87	0.83	0.80	0.78	0.77	0.77	0.77
$\|\cos(\theta_{point})\|_{XY}$	0.998	0.998	0.998	0.998	0.998	0.998	0.998	0.998	0.998	0.998
L_{XY}	7	5	5	5	5	5	8	6	6	6

Table 1 – Looser selection cuts for D^0 of the 10% most central events. These are a variation of the central cuts.

D^0 p_T (GeV/c)	2-3	3-4	4-5	5-6	6-8	8-12	12-16	16-20	20-24	24-∞
Δm_{D_0} (GeV/c^2)	0.400	0.400	0.400	0.400	0.400	0.400	0.400	0.400	0.400	0.400
DCA (cm)	0.0150	0.0150	0.0150	0.0150	0.0200	0.0250	0.0300	0.0300	0.0300	0.0300
$\cos(\theta^*)$	0.8	0.8	0.8	0.8	0.8	1.0	1.0	1.0	1.0	1.0
K p_T (GeV/c)	0.7	0.7	0.7	0.7	0.7	0.7	0.7	0.7	0.7	0.7
π p_T (GeV/c)	0.7	0.7	0.7	0.7	0.7	0.7	0.7	0.7	0.7	0.7
$\|d_0^K\|$ (cm)	1.000	1.000	1.000	1.000	1.000	1.000	1.000	1.000	1.000	1.000
$\|d_0^\pi\|$ (cm)	1.000	1.000	1.000	1.000	1.000	1.000	1.000	1.000	1.000	1.000
$d_0^k d_0^\pi$ (10^{-4} cm^2)	5.1750	4.1400	3.1050	2.4150	1.6100	0.5750	0.1150	0.1150	0.1150	0.1150
$\cos(\theta_{point})$	0.98	0.98	0.98	0.97	0.93	0.90	0.88	0.87	0.87	0.87
$\|\cos(\theta_{point})\|_{XY}$	0.998	0.998	0.998	0.998	0.998	0.998	0.998	0.998	0.998	0.998
L_{XY}	7	5	5	5	5	5	8	6	6	6

Table 2 – Tighter selection cuts for D^0 of the 10% most central events. These are a variation of the central cuts.

D^0 p_T (GeV/c)	2-3	3-4	4-5	5-6	6-8	8-12	12-16	16-20	20-24	24-∞
Δm_{D_0} (GeV/c^2)	0.400	0.400	0.400	0.400	0.400	0.400	0.400	0.400	0.400	0.400
DCA (cm)	0.0300	0.0300	0.0300	0.0300	0.0300	0.0300	0.0300	0.0400	0.0400	0.0400
$\cos(\theta^*)$	0.8	0.8	0.8	0.8	0.8	0.8	0.8	1.0	1.0	1.0
K p_T (GeV/c)	0.6	0.6	0.6	0.7	0.7	0.7	0.7	0.7	0.7	0.7
π p_T (GeV/c)	0.6	0.6	0.6	0.7	0.7	0.7	0.7	0.7	0.7	0.7
$\lvert d_0^K \rvert$ (cm)	0.1	0.1	0.1	0.1	0.1	0.1	0.1	0.1	0.1	0.1
$\lvert d_0^\pi \rvert$ (cm)	0.1	0.1	0.1	0.1	0.1	0.1	0.1	0.1	0.1	0.1
$d_0^k d_0^\pi$ (10^{-4} cm^2)	3.6	3.6	3.6	1.8	1.8	0.50	0.50	1.0	1.0	0.10
$\cos(\theta_{point})$	0.92	0.92	0.92	0.90	0.90	0.85	0.85	0.92	0.92	0.8
$\lvert\cos(\theta_{point})\rvert_{XY}$	0.997	0.997	0.997	0.998	0.998	0.998	0.998	0.995	0.995	0.99
L_{XY}	7	7	7	6	6	5	5	5	5	2

Table 3 – Andrea Rossi's selection cuts for D^0 of the 10% most central events.

Appendix B: Results

In this appendix, the results for the looser, tighter and AR selection cut sets are shown. The following definitions are used for the purple procedure:

- Raw Purple: purple procedure without correction for efficiency.
- Raw Purple with extra D^0 p_T cut: purple procedure without correction for efficiency. For jet $p_T \geq 10$ GeV/c, D^0 p_T bin $[2, 3)$ GeV/c is removed.
- Purple: purple procedure with efficiency correction.
- Purple with extra D^0 p_T cut: purple procedure with efficiency correction. For jet $p_T \geq 10$ GeV/c, D^0 p_T bin $[2, 3)$ GeV/c is removed.

For the orange procedure there are similar definitions:

- Raw Orange: orange procedure without correction for efficiency.
- Raw Orange with extra D^0 p_T cut: orange procedure without correction for efficiency. In D^0 p_T bin $[2, 3)$ GeV/c, contributions of jet $p_T \geq 10$ GeV/c are removed.
- Orange: orange procedure with efficiency correction.
- Orange with extra D^0 p_T cut: orange procedure with efficiency correction. n D^0 p_T bin $[2, 3)$ GeV/c, contributions of jet $p_T \geq 10$ GeV/c are removed.

Commentary on the results can be found in the captions of the figures. The literary value of the mass of the D^0-meson is (1864 ± 0.05) MeV/c^2.

Looser selection cut set

In this section, the results from the purple and orange procedures for the looser selection cut set are presented. Figure 1 shows the invariant mass distributions for the Raw Purple procedure with and without extra D^0 p_T cut. Figure 2 shows the invariant mass distributions for the Purple procedure again with and without extra D^0 p_T cut. The parameters from all versions of the purple procedure are shown in figure 3.

The invariant mass and jet p_T distributions from the orange procedure are shown in figure 4. The invariant mass distributions are the same for all versions of orange. The only difference between the jet p_T distribution of (Raw) Orange and (Raw) Orange with an extra D^0 p_T cut is that the contributions of jet $p_T \geq 10$ GeV/c in D^0 p_T bin $[2, 3)$ GeV/c are removed. The parameters of the Orange procedure (same for all except the final jet p_T spectrum) are shown in figure 5.

The jet p_T distributions are compared in figure 6.

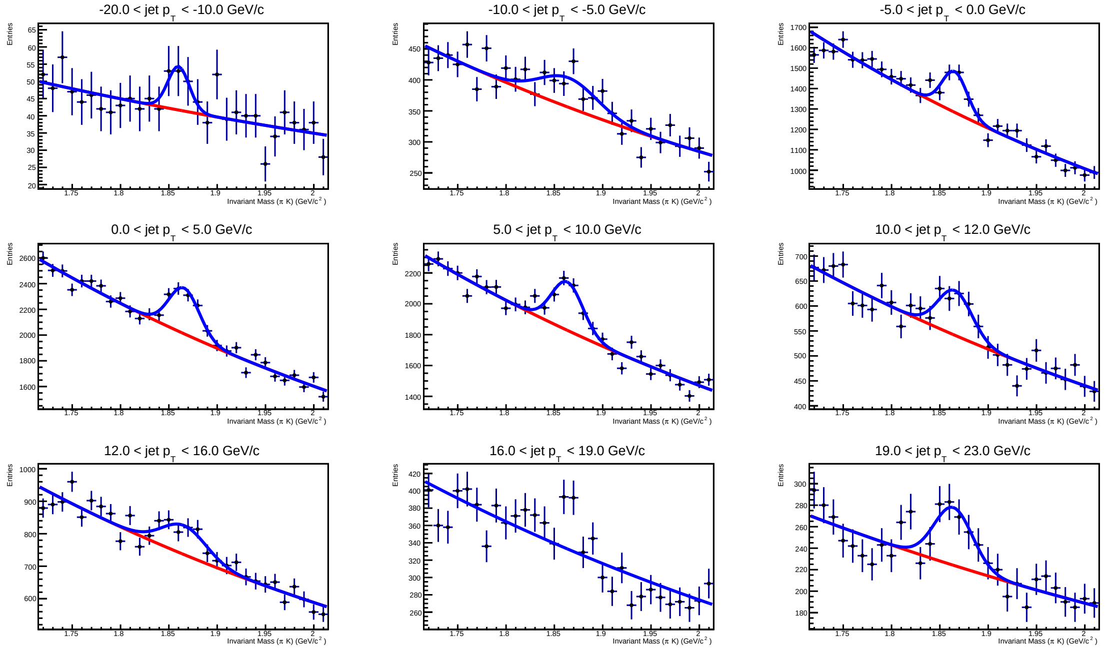

(a) Raw Purple procedure. The fit in bin $[16, 19)$ GeV/c failed.

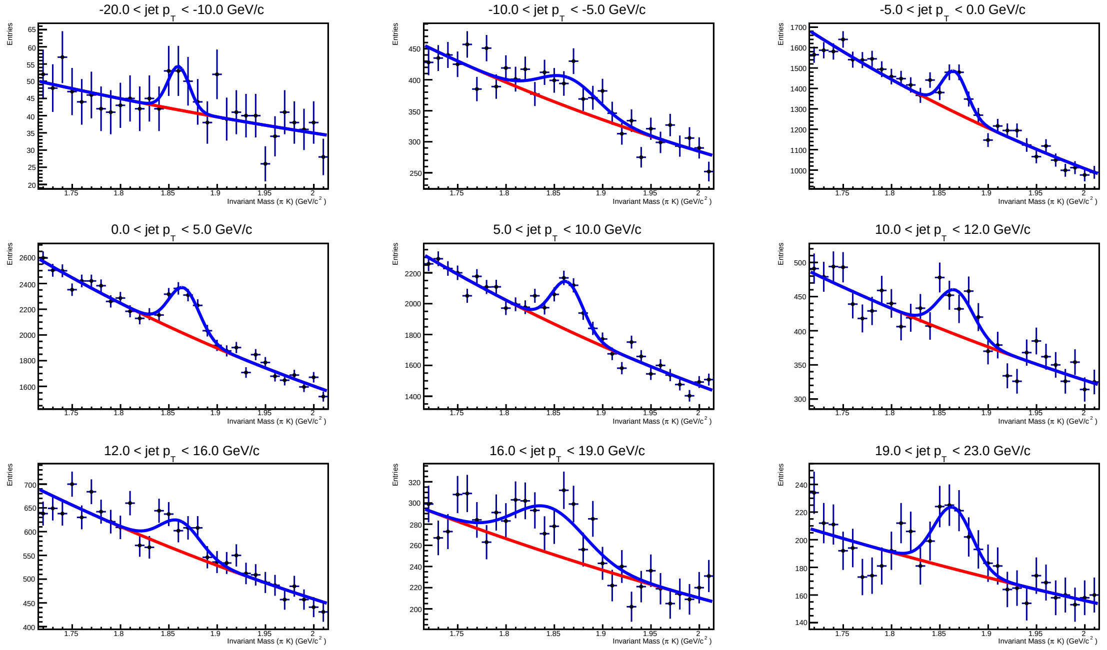

(b) Raw Purple procedure with extra D^0 p_T cut. With the cut, the fit in bin $[16, 19)$ GeV/c did not fail, although the peak is broader than the adjacent bins. This is unusual.

Figure 1 – Invariant mass distributions from the Raw Purple procedure.

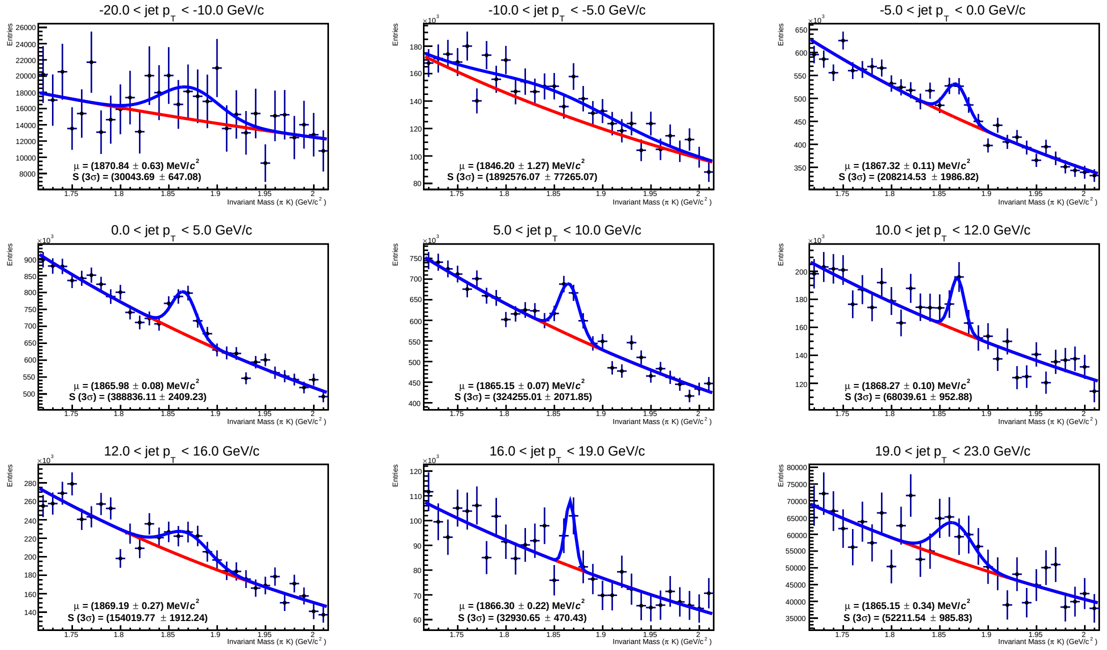

(a) Purple procedure. The peak in bin $[-10, -5)$ GeV/c is unexpectedly flat and broad. The peak in bin $[12, 16)$ GeV/c is broader and lower than in the adjacent bins. The peaks in bins $[10, 12)$ and $[16, 19)$ GeV/c are very sharp.

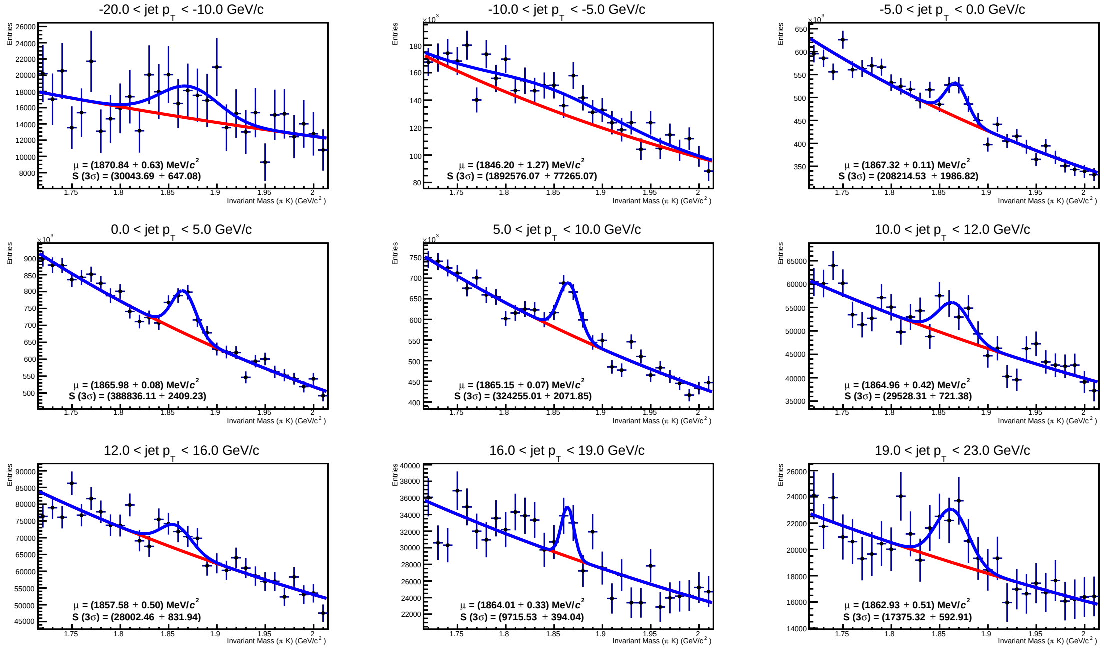

(b) Purple procedure with extra D^0 p_T cut. The cut did not improve the invariant mass distribution in bin $[12, 16)$ GeV/c. The peaks in bins $[10, 12)$ and $[16, 19)$ GeV/c are now less sharp.

Figure 2 – Invariant mass distributions from the Purple procedure.

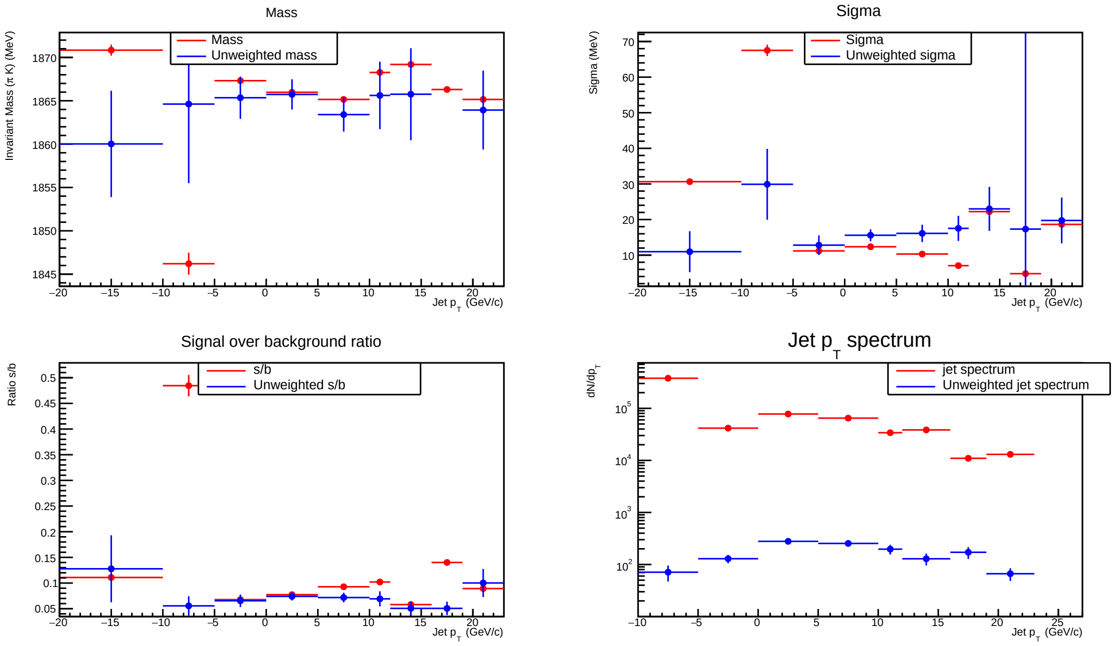

(a) Parameters from the (Raw) Purple procedure. Almost all mass values of the purple procedure deviate from the literary value of D^0 mass, though it is hard to judge due to the small errors. The values of sigma are mostly the same.

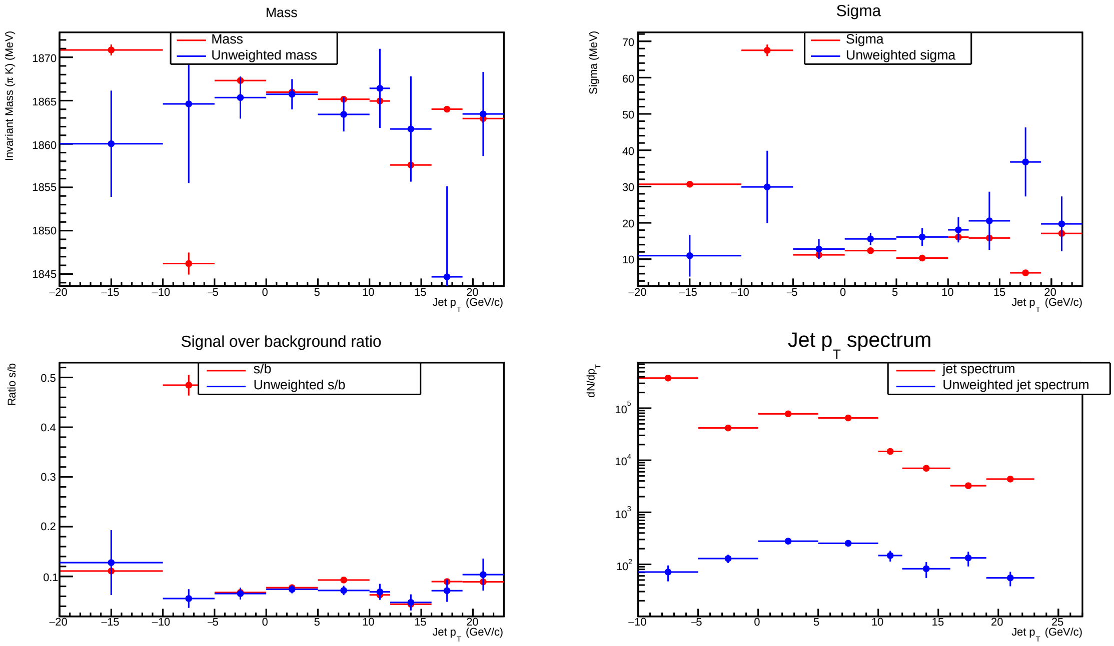

(b) (Raw) Purple procedure with extra D^0 p_T cut. Some mass values from the purple procedure are now around the literary value. Sigma mostly increases. The jet p_T distribution increases at its tail.

Figure 3 – Parameters from the (Raw) Purple procedure with extra D^0 p_T cut. The parameters from Raw Purple are shown in blue; from Purple in red.

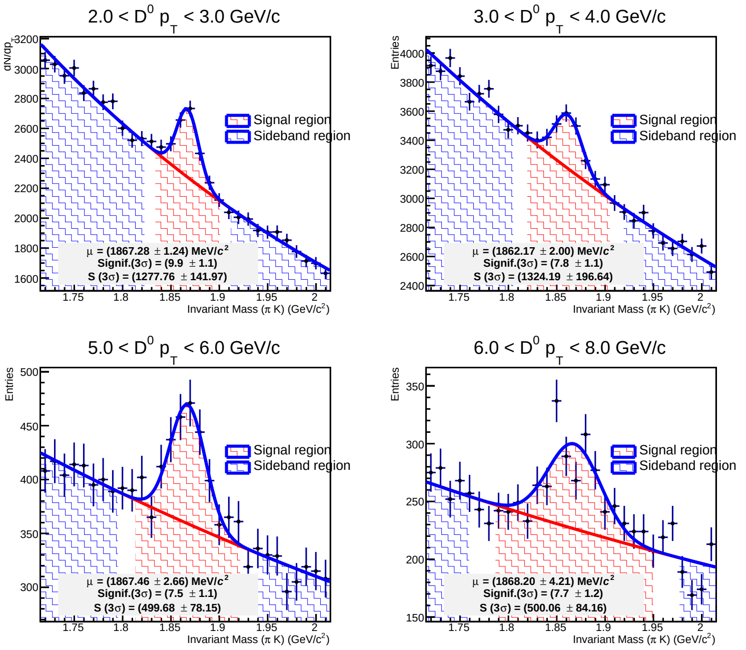

(a) Invariant mass distributions from the orange procedure. This is the same for all defined versions of the orange procedure. The signal peaks are well-defined.

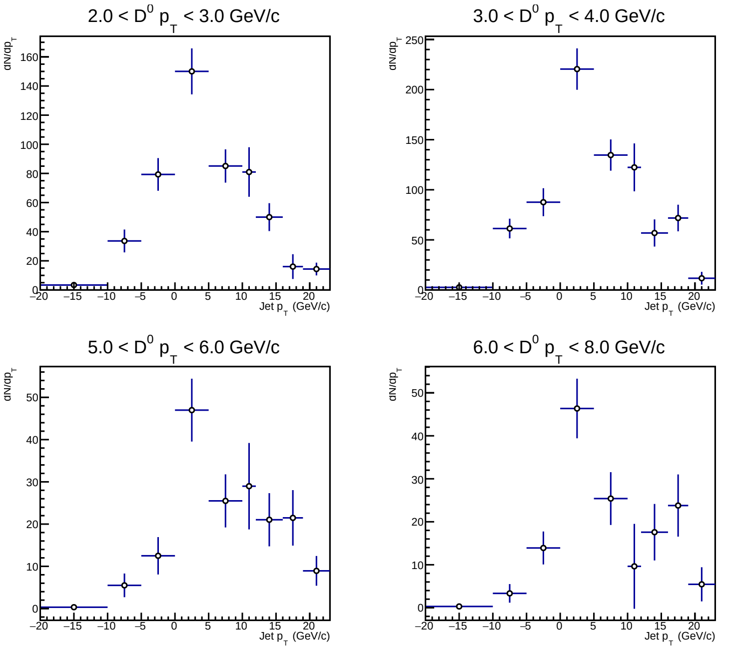

(b) Jet p_T distributions from the Orange procedure. This is the same for Raw Orange. In case of the extra D^0 p_T cut, the contributions of jet $p_T \geq 10$ GeV/c in D^0 p_T bin $[2,3)$ GeV/c are removed. In some D^0 p_T bins, the yield increases rather than decreases for higher jet p_T.

Figure 4 – Invariant mass distributions and jet p_T distributions from the Orange procedure per D^0 p_T bin.

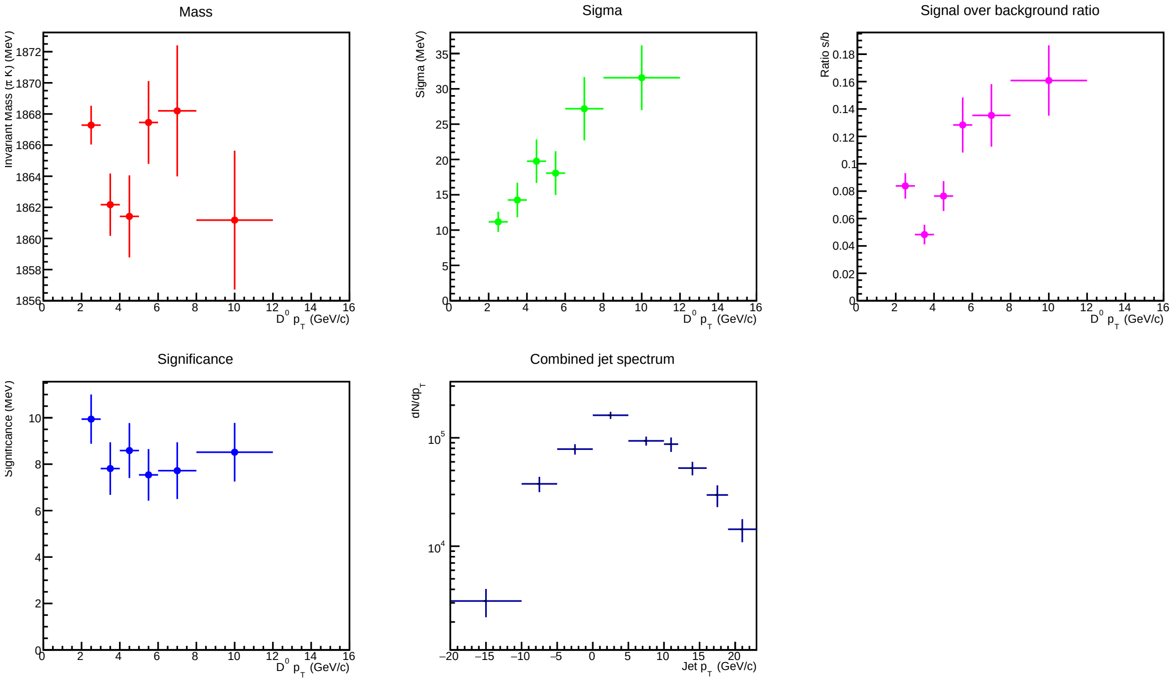

Figure 5 – Parameters from the Orange procedure. Mass, sigma, significance and signal/background ratio are the same for all versions of the Orange procedure. The jet p_T distribution shown is from Orange. The mass entries fluctuate around the literary value. As expected, sigma and s/b ratio increase with D^0 p_T. The significance is well above 3sigma: the mass peaks are relevant.

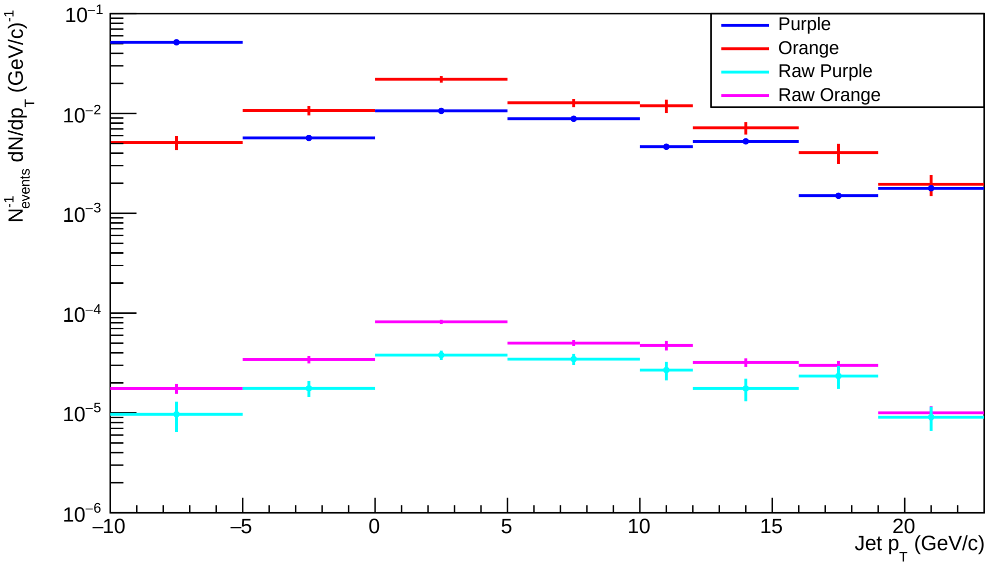

(a) Final jet p_T distributions for (Raw) Purple and (Raw) Orange.

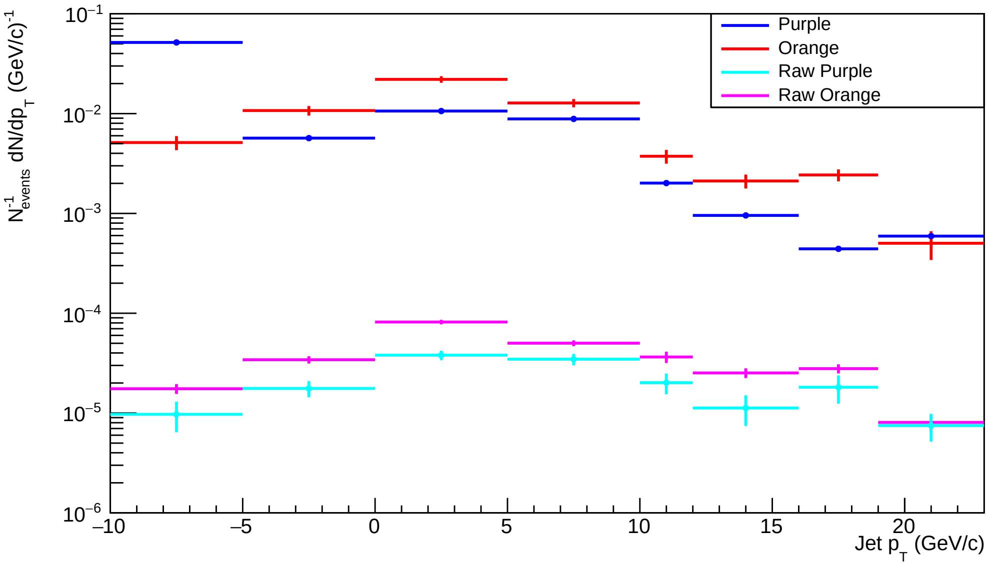

(b) Final jet p_T distributions for (Raw) Purple and (Raw) Orange with extra D^0 p_T cut.

Figure 6 – Comparison of final jet p_T distributions. Shown are: Orange (red), Raw Orange (pink), Purple (blue) and Raw Purple (light blue). There is a clear deviation between the distributions from the orange and purple procedure.

Tighter selection cut set

In this section, the results of from the purple and orange procedures for the tighter selection cut set are presented. Figure 7 shows the invariant mass distributions for the Raw Purple procedure with and without extra D^0 p_T cut. Figure 8 shows the invariant mass distributions for the Purple procedure again with and without extra D^0 p_T cut. The parameters from all versions of the purple procedure are shown in figure 9.

The invariant mass and jet p_T distributions from the orange procedure are shown in figure 10. The invariant mass distributions are the same for all versions of orange. The only difference between the jet p_T distribution of (Raw) Orange and (Raw) Orange with an extra D^0 p_T cut is that the contributions of jet $p_T \geq 10$ GeV/c in D^0 p_T bin $[2, 3)$ GeV/c are removed. The parameters of the Orange procedure (same for all except the final jet p_T spectrum) are shown in figure 11.

The jet p_T distributions are compared in figure 12.

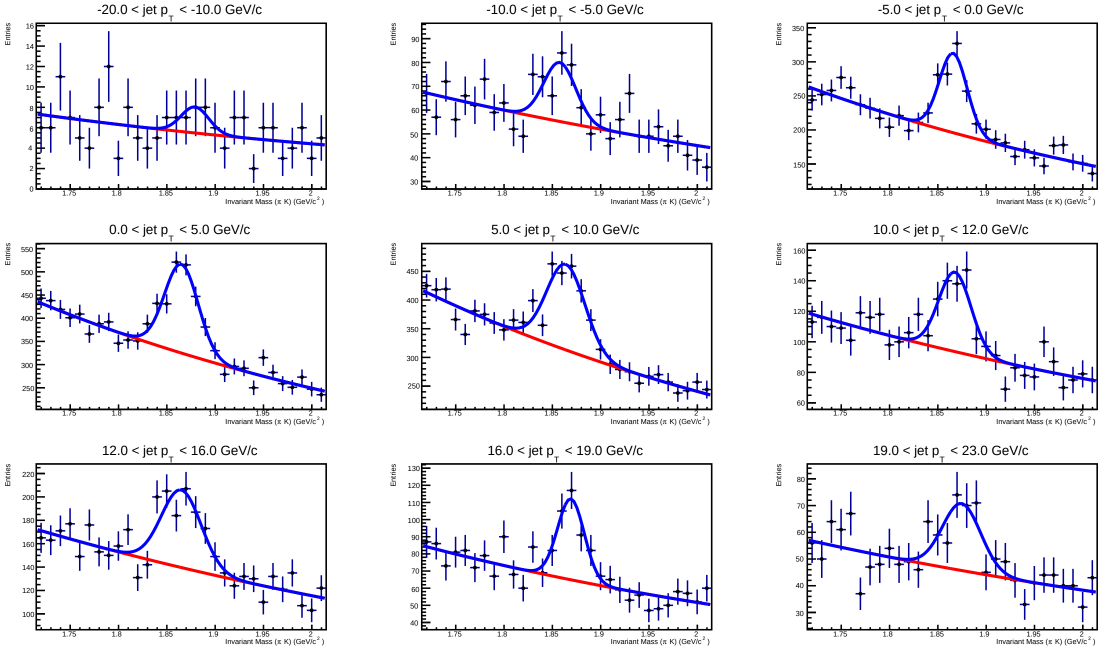

(a) Raw Purple procedure.

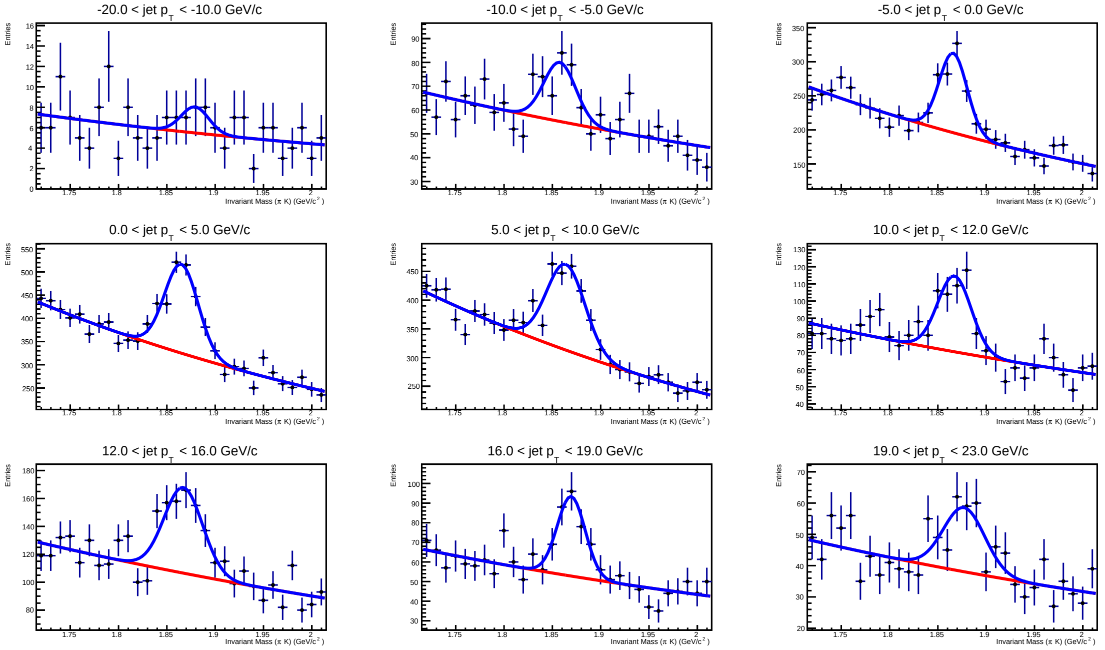

(b) Raw Purple procedure with extra D^0 p_T cut.

Figure 7 – Invariant mass distributions from the Raw Purple procedure. The fits look good.

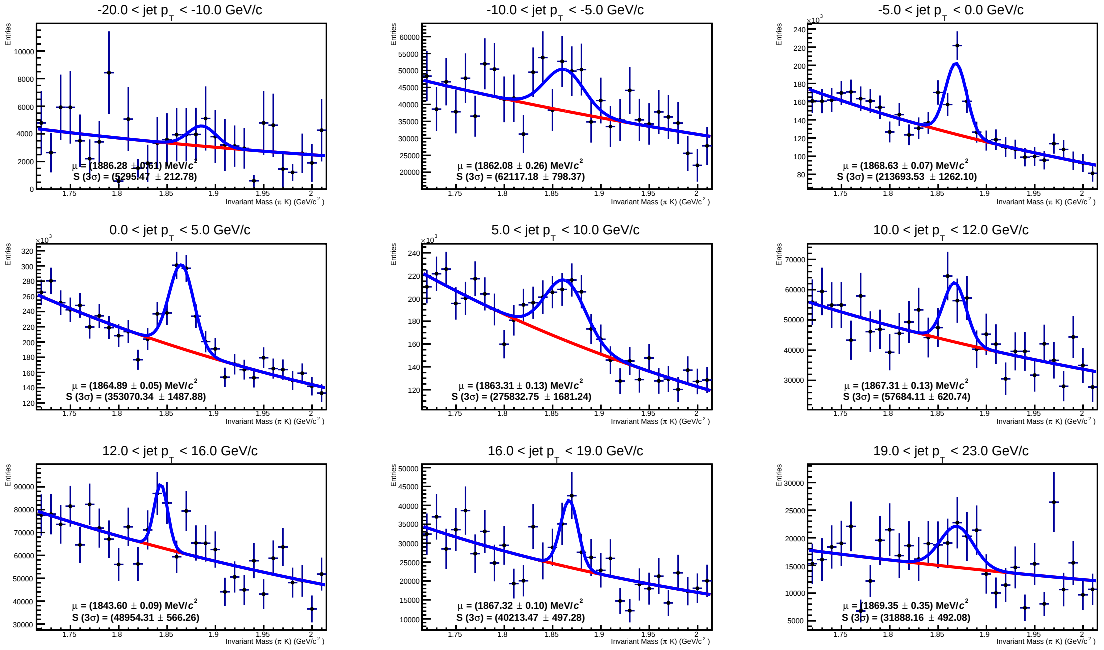

(a) Purple procedure. The peaks in jet p_T range $[12, 19)$ GeV/c are slightly sharper than the adjacent bins. In bin $[19, 23)$ GeV/c one point deviates a lot from the fitted background.

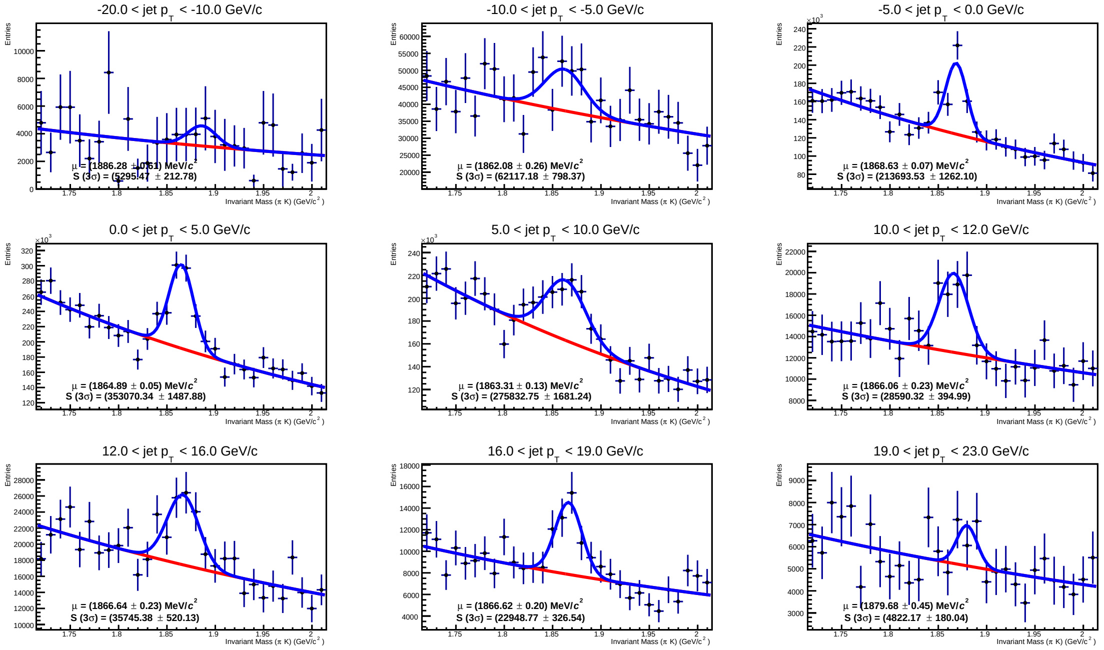

(b) Purple procedure with extra D^0 p_T cut.

Figure 8 – Invariant mass distributions from the Purple procedure. The peaks in range $[12, 19)$ GeV/c are now more like the peaks in the neighbouring bins. The deviating entry in bin $[19, 23)$ GeV/c now fits more with the background.

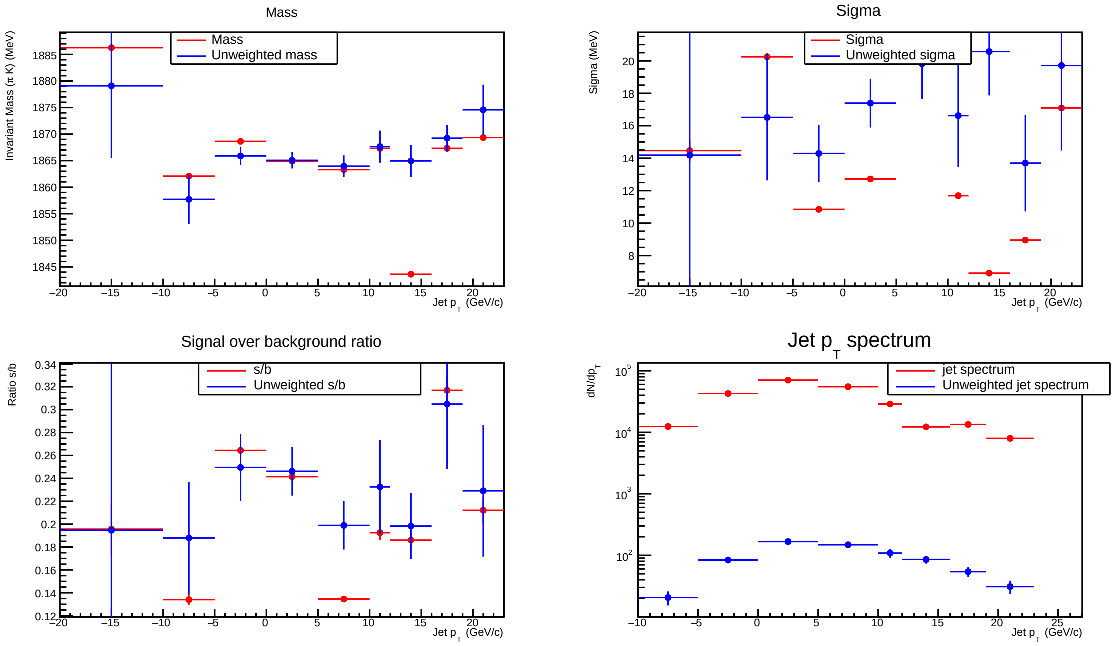

(a) Parameters from the (Raw) Purple procedure. The mass entry in bin $[-20, -10)$ GeV/c deviates by a large amount from the literary mass of D^0. The mass in the higher jet p_T bins also deviate. Sigma and the s/b ratio fluctuate a lot.

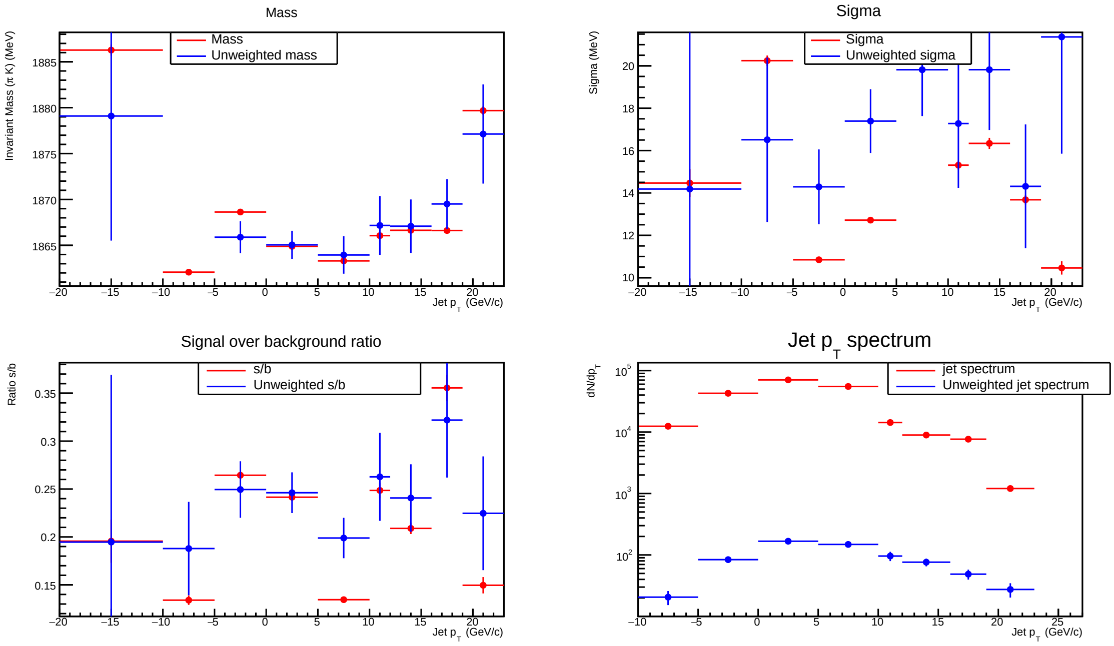

(b) (Raw) Purple procedure with extra D^0 p_T cut. The mass entries for higher jet p_T are still too high. Sigma and the s/b ratio still fluctuate.

Figure 9 – Parameters from the (Raw) Purple procedure with extra D^0 p_T cut. The parameters from Raw Purple are shown in blue; from Purple in red.

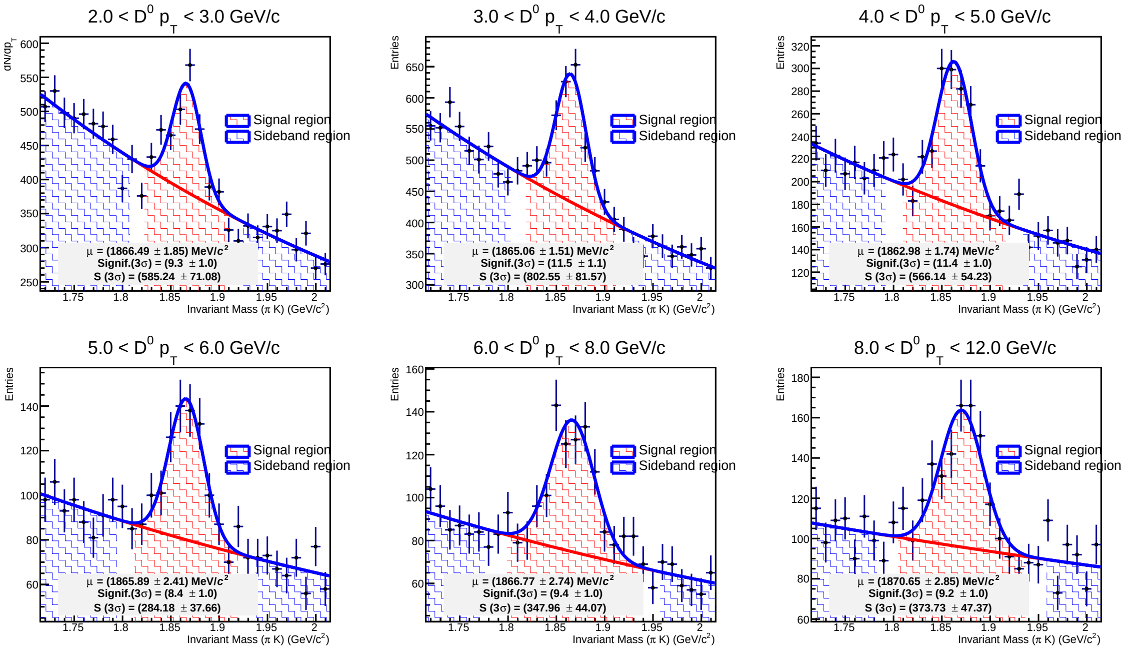

(a) Invariant mass distributions from the orange procedure. This is the same for all defined versions of the orange procedure.

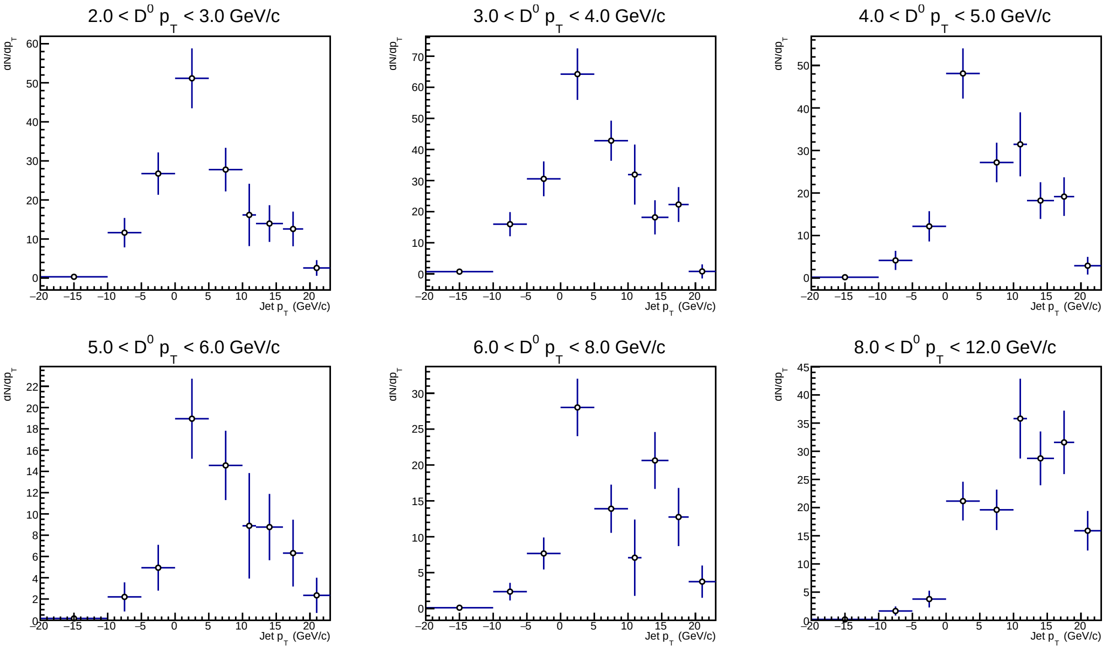

(b) Jet p_T distributions from the Orange procedure. This is the same for Raw Orange. In case of the extra D^0 p_T cut, the contributions of jet $p_T \geq 10$ GeV/c in D^0 p_T bin $[2, 3)$ GeV/c are removed. The higher D^0 p_T bins contain relatively more entries to high jet p_T bins.

Figure 10 – Invariant mass distributions and jet p_T distributions from the Orange procedure per D^0 p_T bin.

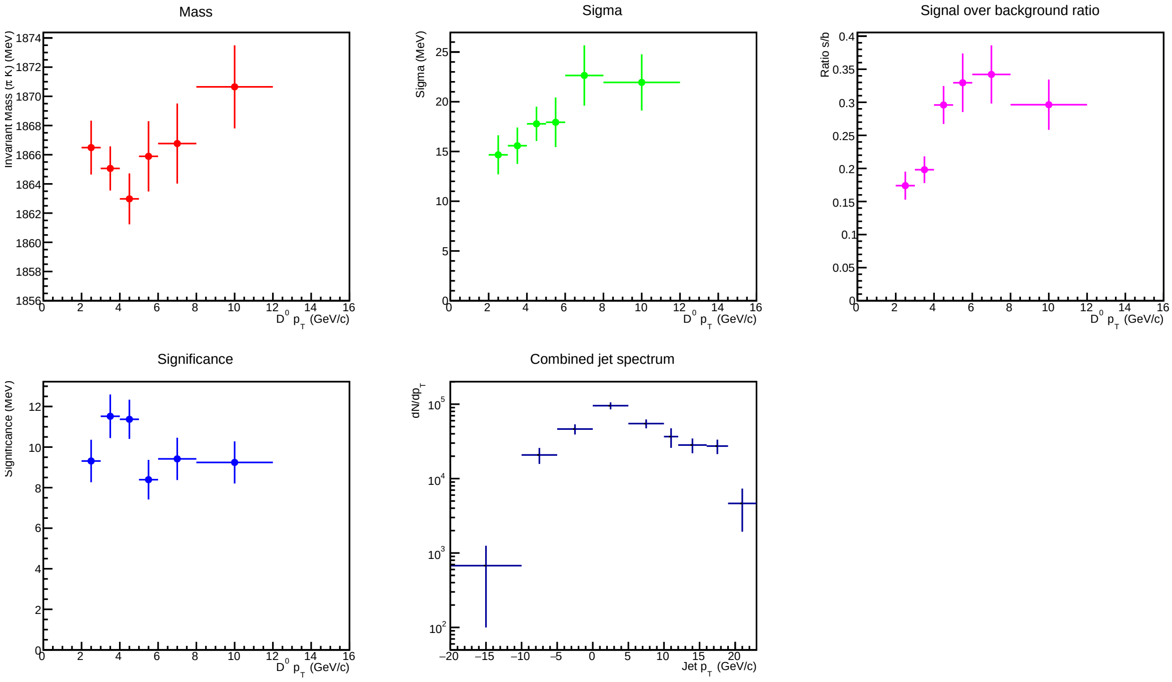

Figure 11 – Parameters from the Orange procedure. Mass, sigma, significance and signal/background ratio are the same for all versions of the Orange procedure. The jet p_T distribution shown is from Orange. The entries in the mass histogram are higher than the literary mass of D^0. Sigma and s/b ratio mostly increase. The significance is above 3 sigma, meaning the invariant masses found are relevant.

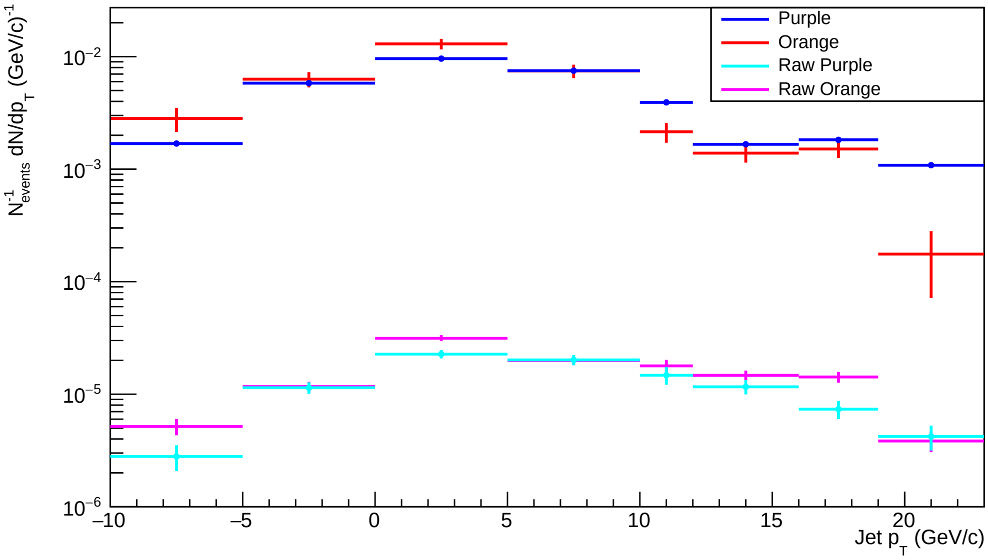

(a) Final jet p_T distributions for (Raw) Purple and (Raw) Orange.

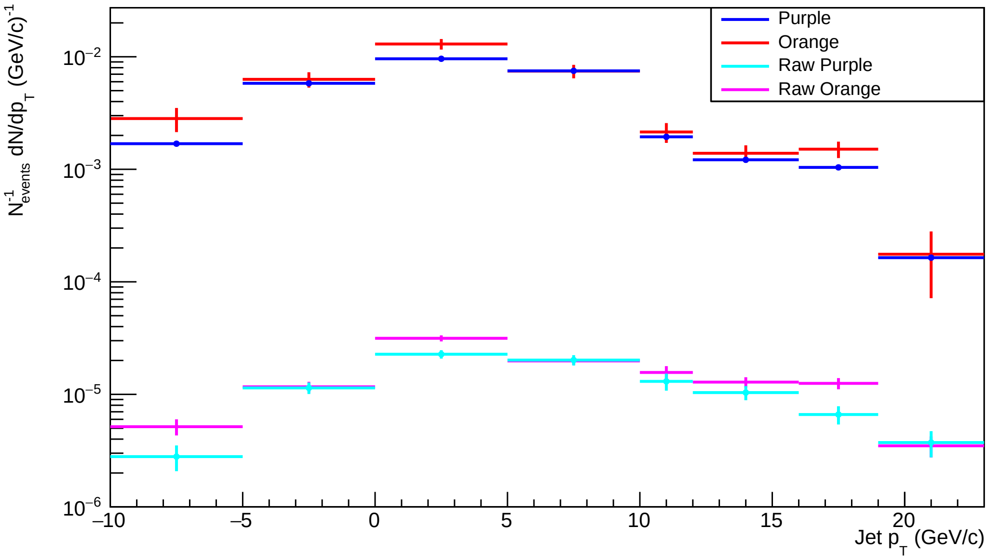

(b) Final jet p_T distributions for (Raw) Purple and (Raw) Orange with extra D^0 p_T cut.

Figure 12 – Comparison of final jet p_T distributions. Shown are: Orange (red), Raw Orange (pink), Purple (blue) and Raw Purple (light blue). The additional D^0 p_T cut has improved the consistency between the purple and orange procedure.

AR selection cut set

In this section, the results of from the purple and orange procedures for the AR selection cut set are presented. Figure 13 shows the invariant mass distributions for the Raw Purple procedure with and without extra D^0 p_T cut. Figure 14 shows the invariant mass distributions for the Purple procedure again with and without extra D^0 p_T cut. The parameters from all versions of the purple procedure are shown in figure 15.

The invariant mass and jet p_T distributions from the orange procedure are shown in figure 16. The invariant mass distributions are the same for all versions of orange. The only difference between the jet p_T distribution of (Raw) Orange and (Raw) Orange with an extra D^0 p_T cut is that the contributions of jet $p_T \geq 10$ GeV/c in D^0 p_T bin $[2, 3)$ GeV/c are removed. The parameters of the Orange procedure (same for all except the final jet p_T spectrum) are shown in figure 17.

The jet p_T distributions are compared in figure 18.

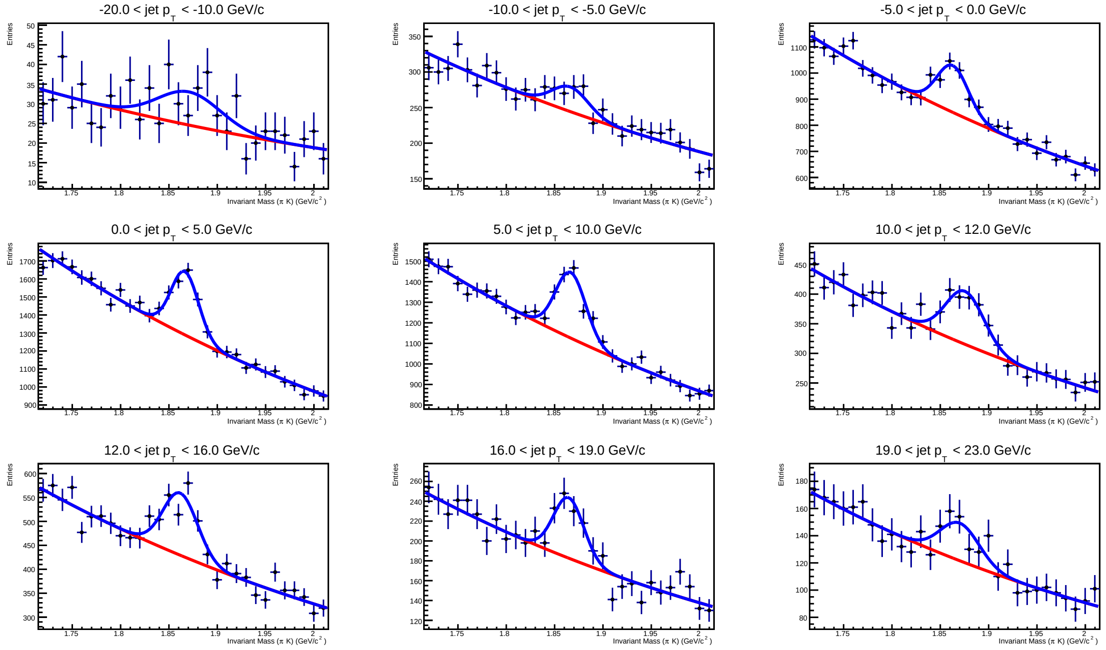

(a) Raw Purple procedure.

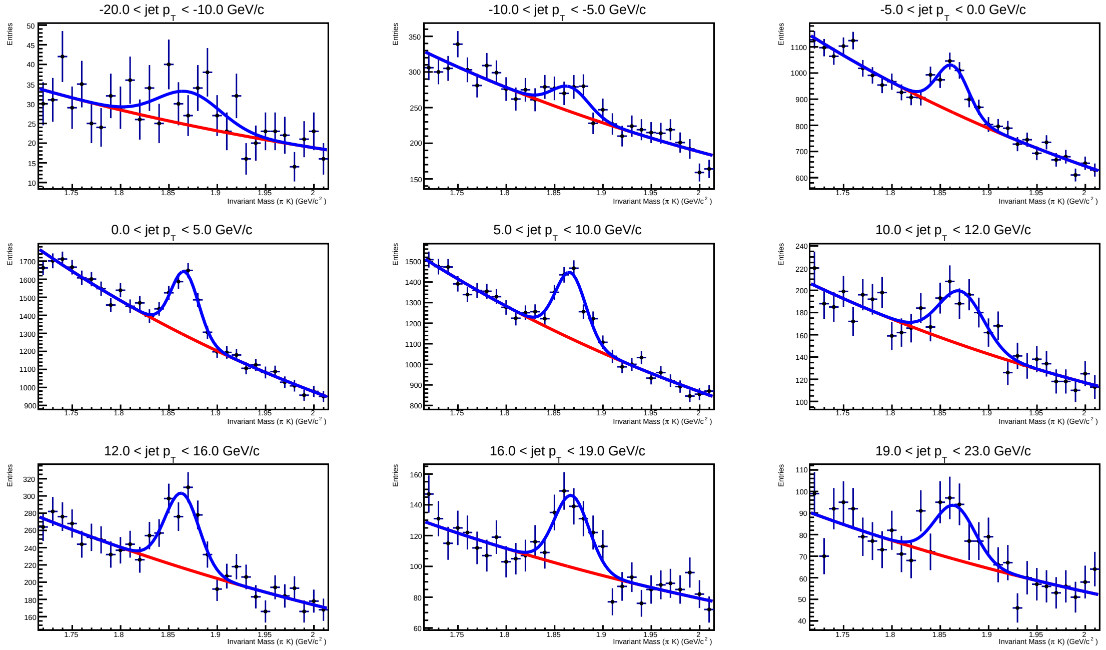

(b) Raw Purple procedure with extra D^0 p_T cut.

Figure 13 – Invariant mass distributions from the Raw Purple procedure. The distributions from jet p_T bins $[-20, -5)$ GeV/c are flatter and broader than the other peaks.

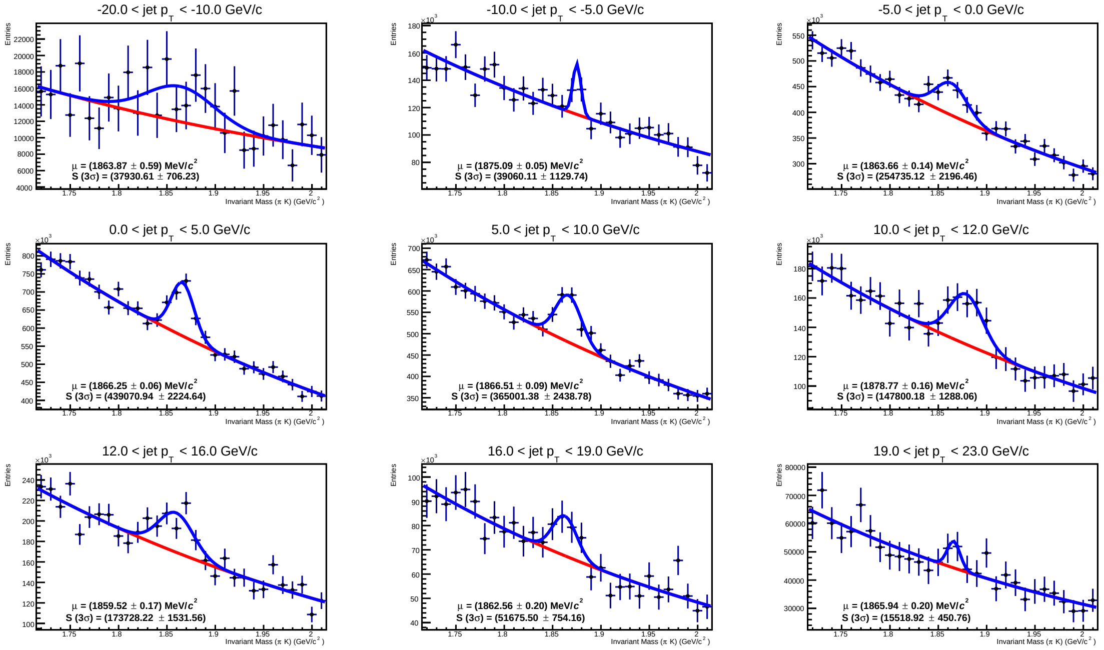

(a) Purple procedure. The mass peaks in jet p_T range $[-20, 0)$ GeV/c are either sharper or flatter than expected; the same is true for bin $[19, 23)$ GeV/c. The mass peak in the latter bin is also very small.

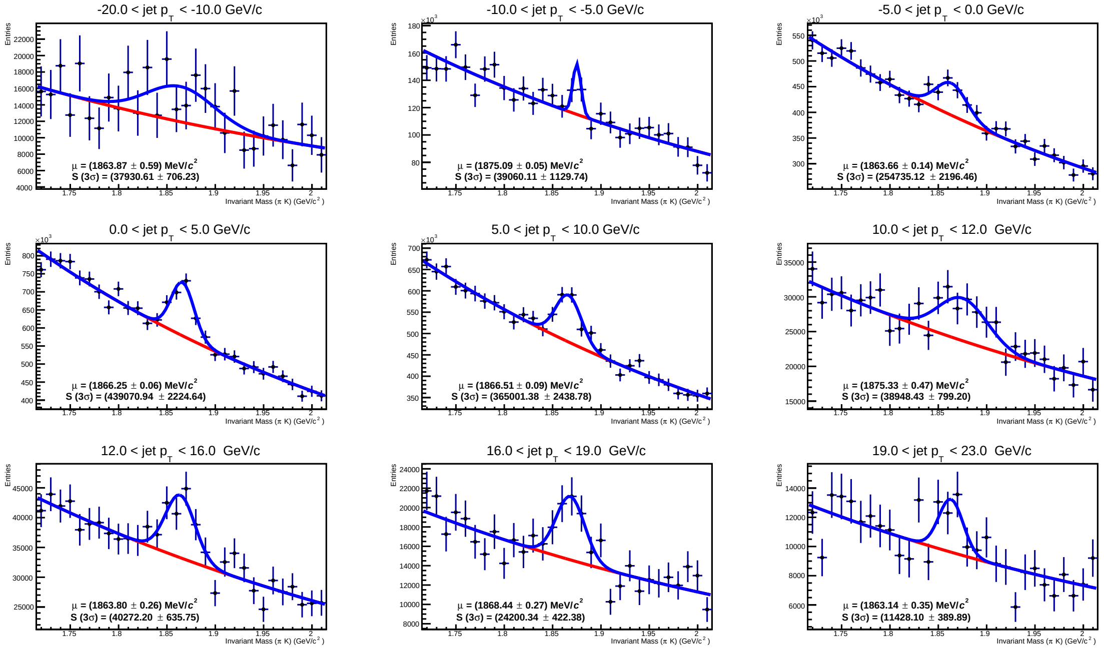

(b) Purple procedure with extra D^0 p_T cut. The cut has improved the height of the peaks. They are now more distinguished from the background.

Figure 14 – Invariant mass distributions from the Purple procedure.

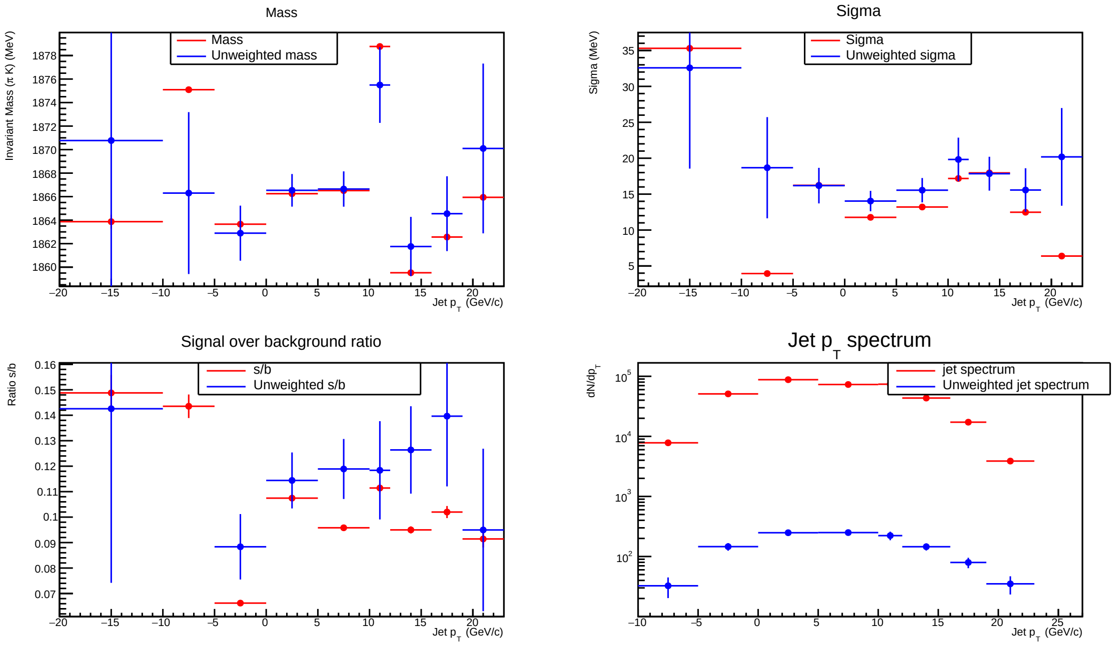

(a) Parameters from the (Raw) Purple procedure. Most entries in the mass histogram are around the invariant mass histogram. The biggest deviation is in the first bin and in bin $[12, 16)$ GeV/c. Sigma and s/b ratio fluctuate a lot.

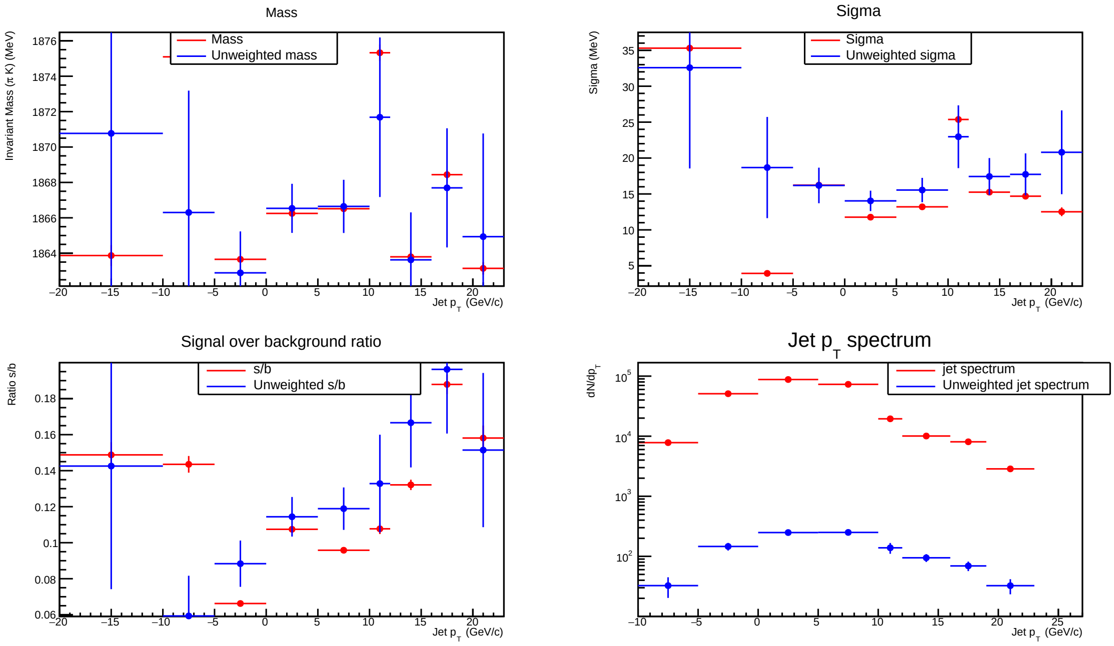

(b) (Raw) Purple procedure with extra D^0 p_T cut. All parameters fluctuate. The last entry in the mass histogram has actually deteriorated.

Figure 15 – Parameters from the (Raw) Purple procedure with extra D^0 p_T cut. The parameters from Raw Purple are shown in blue; from Purple in red.

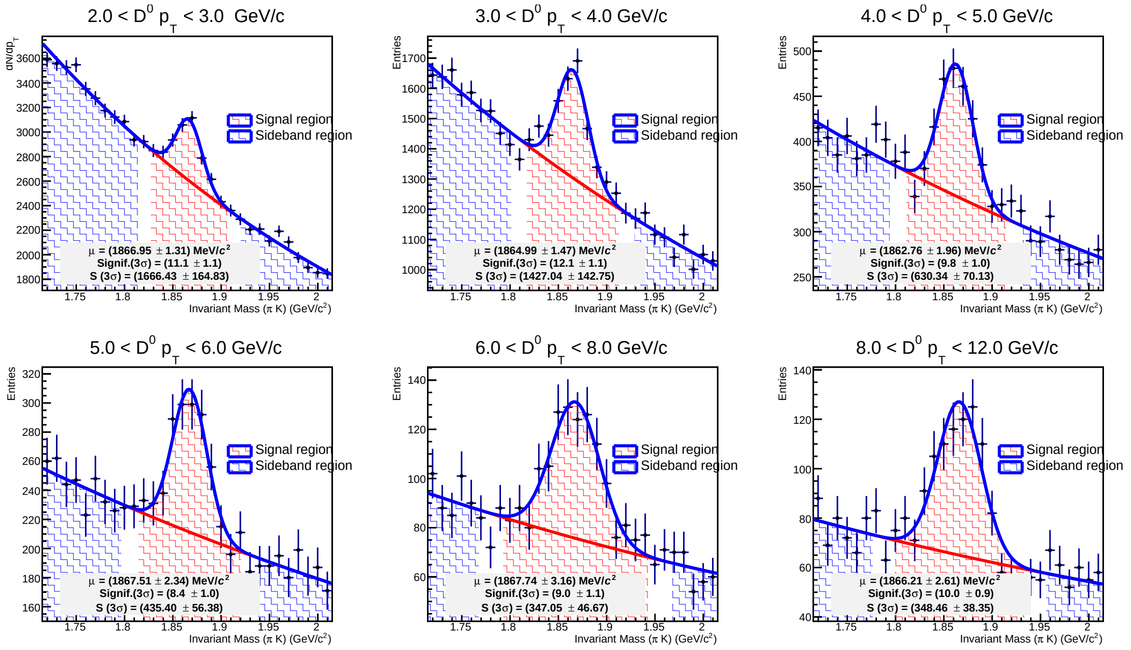

(a) Invariant mass distributions from the orange procedure. This is the same for all defined versions of the orange procedure.

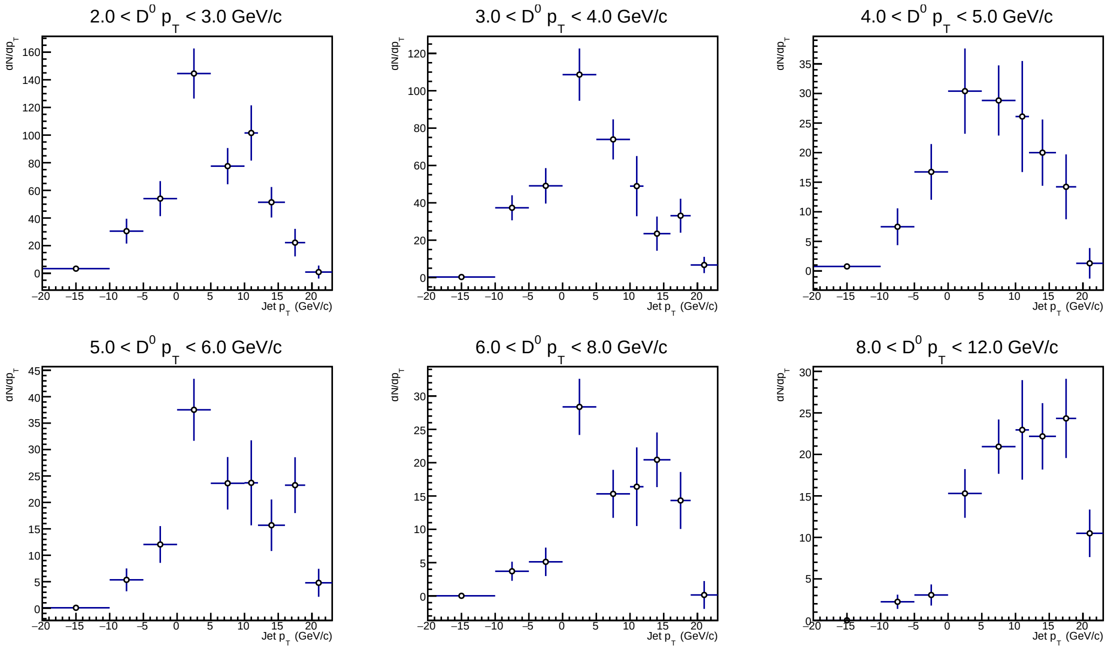

(b) Jet p_T distributions from the Orange procedure. This is the same for Raw Orange. In case of the extra D^0 p_T cut, the contributions of jet $p_T \geq 10$ GeV/c in D^0 p_T bin $[2, 3)$ GeV/c are removed.

Figure 16 – Invariant mass distributions and jet p_T distributions from the Orange procedure per D^0 p_T bin.

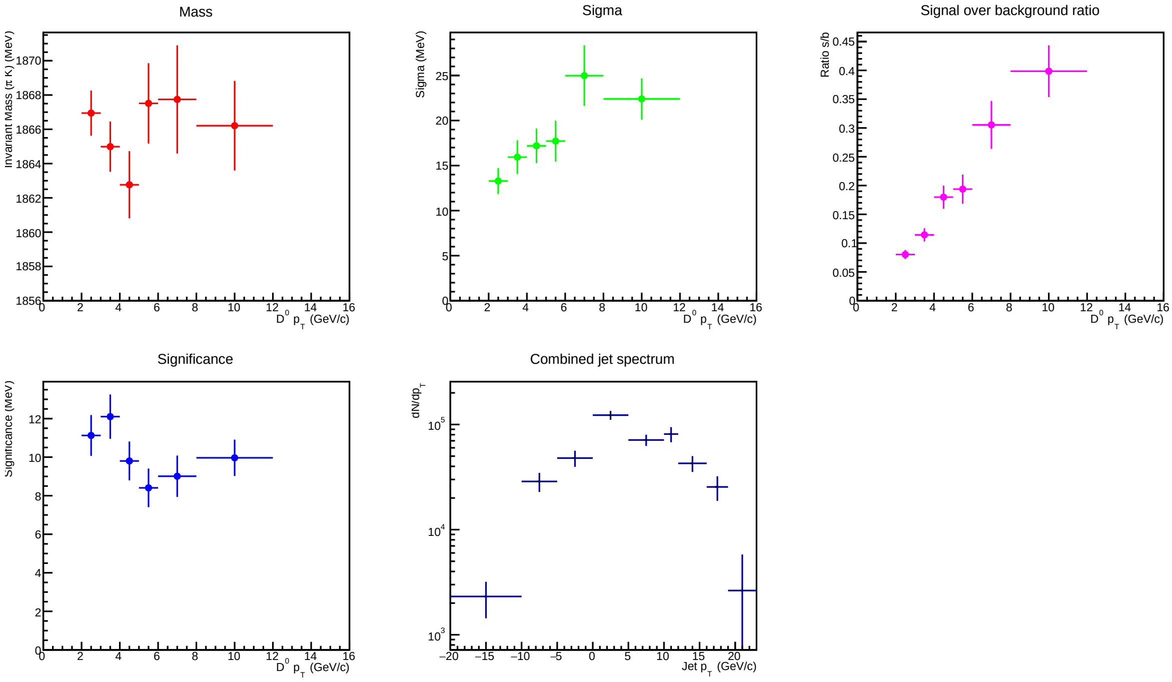

Figure 17 – Parameters from the Orange procedure. Mass, sigma, significance and signal/background ratio are the same for all versions of the Orange procedure. The jet p_T distribution shown is from Orange. Most mass entries are within range of error of the literary D^0 mass. As expected, sigma and s/b ratio mostly increase. The significance is above 3 sigma, meaning that the invariant mass peaks found are relevant.

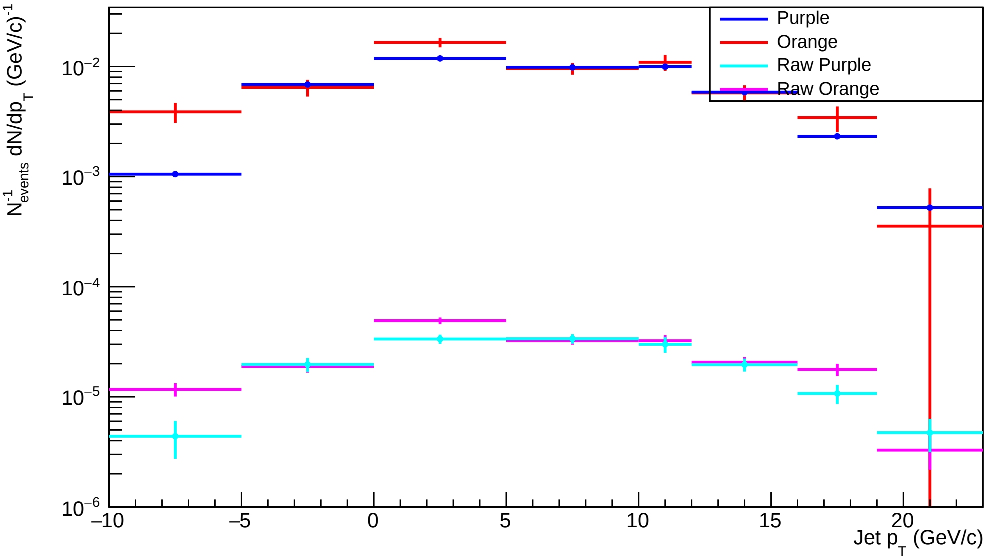

(a) Final jet p_T distributions for (Raw) Purple and (Raw) Orange.

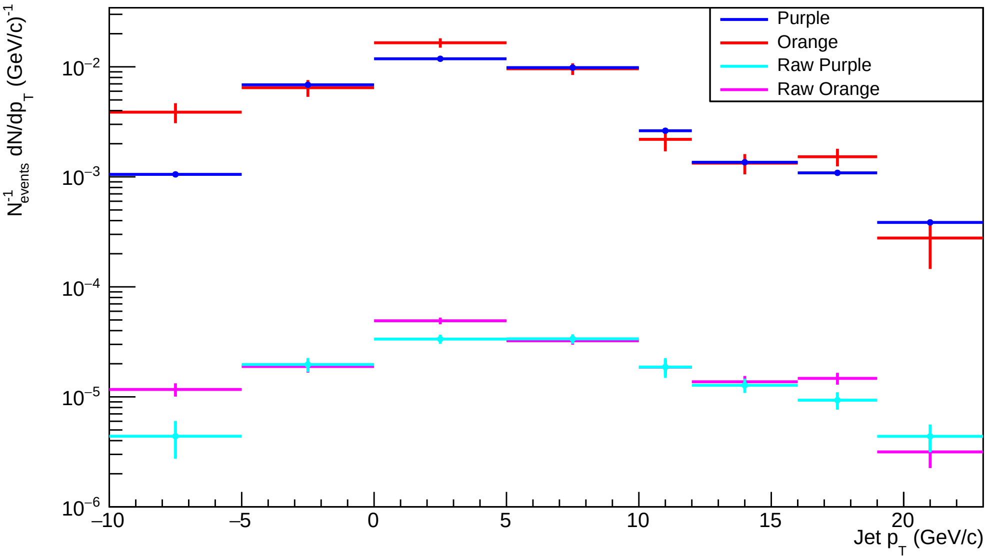

(b) Final jet p_T distributions for (Raw) Purple and (Raw) Orange with extra D^0 p_T cut.

Figure 18 – Comparison of final jet p_T distributions. Shown are: Orange (red), Raw Orange (pink), Purple (blue) and Raw Purple (light blue). The additional D^0 p_T cut improved the consistency of the purple and orange procedures.